

Mechanical and thermal stability of Bulk Metallic Glass alloys identified as candidates for space mechanism applications

A.G. Murphy ^{a,b}, P. Meagher ^b, A. Norman ^c, D.J. Browne ^{b,*}

^a Department of Aerospace and Mechanical Engineering, South East Technological University, Kilkenny Road, Carlow, R93 V960, Ireland

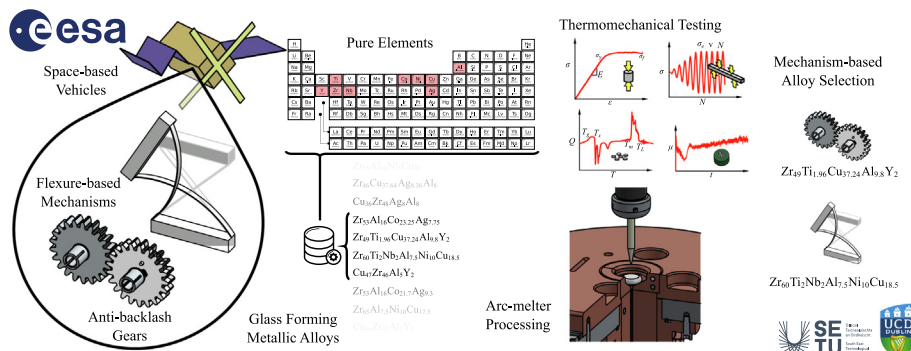
^b School of Mechanical and Materials Engineering, University College Dublin, Belfield Campus, Dublin 4, Ireland

^c European Space Agency, Keplerlaan 1, PO Box 299, NL-2200 AG Noordwijk, the Netherlands

HIGHLIGHTS

- Bulk amorphous alloy compositions are identified as potential materials for applications in space.
- They may be suited to gear and flexure mechanisms, at temperatures up to 400 °C.
- The alloys are formulated and tested for strength, fatigue and thermal stability.
- One bulk metallic glass (BMG) alloy is chosen for anti-backlash gears, another for elastic flexures.
- The BMG properties are competitive with conventional alloys qualified for space.

GRAPHICAL ABSTRACT



ARTICLE INFO

Article history:

Received 30 August 2022

Revised 24 October 2022

Accepted 5 November 2022

Available online 8 November 2022

Keywords:

Fatigue
Stress/strain measurements
Thermal analysis
Amorphous materials
Design of space components
Plasticity

ABSTRACT

Extraterrestrial environments expose engineering components to severe operating conditions for extended durations. Challenges of extreme temperature changes and high vacuum are being met by careful selection of available materials or by development of novel high-performance materials and processes. Bulk Metallic Glasses (BMGs) are amorphous alloys that exhibit very high strengths, hardness, strain energy storage, corrosion resistance, and the capacity for thermoplastic formability, and are of interest in space engineering design. Using criteria driven by the requirements of specific space-based mechanisms, BMG alloys were selected from the literature for processing and performance evaluation. Alloys particularly suited for gearing applications and flexure-based compliant mechanisms were identified and standard test specimens produced. Four Zr-based BMG alloys were selected for analysis: Zr₅₃Al₁₆Co_{23.25}Ag_{7.75}, Cu₄₇Zr₄₆Al₅Y₂, Zr₄₉Ti_{1.96}Cu_{37.24}Al_{9.8}Y₂, and Zr₆₀Ti₂Nb₂Al_{7.5}Ni₁₀Cu_{18.5}, with compositions in at.%. Presented in this work are the results of compression testing, fatigue testing, and differential scanning calorimetry; previous results of wear and hardness testing have been presented elsewhere. A maximum space service temperature of 400 °C is considered. The alloys exhibited significant differences in processability and thermomechanical performance. The alloy Zr₄₉Ti_{1.96}Cu_{37.24}Al_{9.8}Y₂ exhibited the best overall performance for gearing applications; and Zr₆₀Ti₂Nb₂Al_{7.5}Ni₁₀Cu_{18.5} was the best alloy for compliant flexures.

© 2022 The Authors. Published by Elsevier Ltd. This is an open access article under the CC BY-NC-ND license (<http://creativecommons.org/licenses/by-nc-nd/4.0/>).

* Corresponding author.

E-mail address: david.browne@ucd.ie (D.J. Browne).

1. Introduction

Engineering mechanism components such as shafts, gears, bearings, springs, and struts, are used extensively in space vehicles. These components are required to exhibit performance far exceeding their terrestrial counterparts. High vacuum, cosmic radiation, space debris, vibration, extreme and rapidly changing temperatures, varying g-levels, are all design aspects that need to be considered [1,2]. Materials performance criteria for space applications usually include high specific stiffness and strength, fracture toughness, fatigue resistance, thermal expansion coefficient and conductivity, and ease of manufacture [2,3]. For mechanisms that incorporate strain energy storage, e.g., springs and compliant flexures, the maximum stored elastic energy per unit mass is of particular interest [4,5]. Space applications for which compliant mechanisms are needed include deployable, pointing/oscillating, landing, and suspension systems, and vibration isolation [5].

Metallic glasses, discovered more than 60 years ago [6,7], are amorphous, multicomponent, metal alloys. A number of comprehensive reviews on the potential structural applications of bulk metallic glasses (BMGs) have been published over the years [8–11], as well as several books covering a wide range of BMG-related subjects [12,13]. Their amorphous atomic configuration gives them their unique thermomechanical properties. BMGs have been shown to exhibit exceptional strengths, hardness, wear resistance, elastic strain limits, soft/hard magnetic properties, and nano-scale feature replication [14,15]. Since their discovery, the number of metallic glass compositions developed has grown considerably [14,16,17]. Significant milestones including the first commercialization of metallic glass alloys for transformer cores [18], the discovery and development of glass forming Zr-based BMG alloys [19], the commercialization of Zr-based alloys by Liquid-metal® Technologies (CA, USA) under the name Vitrelloy 1 [20], the creation of large Pd-Cu-Ni-P BMG cast volumes [21], ultra-high strength Co-based BMG [22], and ultra-tough BMG matrix composites (BMGMC) [23]. The number of BMGs discovered to date lies in the thousands [16], with potentially millions yet to be investigated. Moreover, thousands of patents have been filed for specific BMG compositions and composition families [17]. However, despite the apparent advantages of BMG alloys over traditional engineering metals, they have found few practical applications due to their apparent brittleness in tensile failure, offering low resistance to crack propagation [24]. They exhibit low ductility and strain softening, causing shear induced inhomogeneous deformation concentrated along narrow shear bands [25]. The propagation of these shear bands leads to crack formation and growth and ultimately failure. However, where section thicknesses of BMG flexures approach the length scale of the processing zone, the zone of plasticity ahead of a propagating crack, significant ductility can be achieved via nucleation of more shear bands [26,27]. Strategies aimed at increasing the number of shear band nucleation events without modifying geometry include the development of BMG matrix composites (BMGMCs), which are a composite of an amorphous matrix and some other reinforcing phase [23,28,29]. BMGMC alloys exhibiting high strength, toughness, and low density have shown potential for structural applications in aerospace and space industries [28]. Many BMG alloys have poor fatigue performance due to a combination of processing defects and the intrinsic nature of the amorphous structure [13,30]. Studies of Zr-based BMG alloys have shown extremely poor fatigue performance [31], which is further compounded by significant variation reported for ostensibly the same material using different testing configurations [31–33]. However some BMG compositions have shown excellent fatigue performance, e.g., $Zr_{50}Cu_{20}Ni_{10}Al_{10}$, Zr_{50}

$Cu_{37}Al_{10}Pd_3$, and $Zr_{52.5}Cu_{17.9}Ni_{14.6}Al_{10}Ti_5$ [33–35]. BMGMC alloys exhibiting excellent fatigue performance have also been developed [36,37]. While promising improvements in the fatigue performance of BMGs have been achieved [38], our study of previous work shows that a generalized view of BMG fatigue performance is not within reach.

Space-based applications for BMGs has gained considerable attention recently [39]. Studies have been published on ultra-smooth and castable mirrors for space-based optics [40], metallic glass coatings for space telescopes [41], spacecraft shielding employing the thermoplastic formability of BMGs [42–44], precision gearing systems for rovers and satellites [45], and spacecraft mechanical locating systems [46]. Bulk metallic glasses have also been characterized for demise during re-entry in satellite applications [47], and have found use in solar wind collectors on board the Genesis mission [48,49]. Thermophysical characterization of BMGs in microgravity in the materials science laboratory onboard the ISS have also been performed [50].

In this work, BMG compositions that satisfied the thermomechanical requirements of specific space-based mechanisms were selected from the literature. The mechanisms of interest are anti-backlash gears and cross-axis large angle flexures. Selected alloys were produced under laboratory conditions and their thermal and mechanical properties characterized. Test specimens were produced to evaluate the processability, thermal, and mechanical properties of each alloy system. Compositions exhibiting a combination of processability, and the desired thermomechanical properties, will form the subject of follow-up mechanism testing under practical space conditions.

2. Materials, equipment and methods

Over 100 BMG alloy compositions were originally considered for the space mechanisms identified and, as per the criterial review previously reported [51], the list was shortened to 4 alloys based on their properties as reported in the literature. The database of compiled BMG alloys presented by Li et al. [16] was used as a starting point for selecting potential BMG compositions exhibiting appropriate thermomechanical properties for selected mechanisms that operate in the space environment. The mechanisms of interest were small (e.g., PCD 20 mm, MOD 0.8 mm) anti-backlash gears and large angle cross axis flexures. The small gear dimension and thin flexures allowed for the selection of glass forming alloys with moderate critical casting diameters, i.e., ≥ 10 mm. Further selection criteria were the use of relatively low-cost pure elements and non-beryllium containing compositions. While the addition of beryllium greatly improves the glass forming of many alloys, its toxicity makes processing hazardous. Finally, alloys comprising elements that could be processed using a standard arc melter were down selected (Al, Ti, Fe, Co, Ni, Cu, Y, Zr, Nb, Ag, and Hf), resulting in approximately 35 suitable compositions. The most common family of BMG alloys at this stage of the selection process was the Zr-Cu-Al system, with minor variations in the at.% of constituent elements, and addition of between one and six extra elements. The four BMG compositions that are the focus of this work are $Zr_{53}Al_{16}Co_{23.25}Ag_{7.75}$ [52], $Zr_{49}Ti_{1.96}Cu_{37.24}Al_{9.8}Y_2$ [53], $Zr_{60}Ti_2Nb_2Al_{7.5}Ni_{10}Cu_{18.5}$ [54], and $Cu_{47}Zr_{46}Al_5Y_2$ [55].

The selected BMG alloys were characterized for strength, fatigue endurance, thermoplastic formability, and high temperature operating range. Details of results describing the wear resistance and hardness of each of the selected alloy compositions, along with comparisons with traditional engineering metals used in space applications, have already been presented in the literature [51]. Note all alloy compositions are expressed in units of at.% throughout this article. These Zr-based alloy systems reportedly exhibited

suitable thermomechanical properties and critical casting diameters required to have potential for the selected mechanisms.

2.1. BMG alloy synthesis and validation

A complete description of the BMG synthesis methodology used in this work has already been presented in the literature [51]. BMG alloys were manufactured from high purity elements: Zr (99.97 %), Cu (99.99 %), Al (99.9995 %), Ag (99.99 %), Ti (99.98 %), Y (99.9 %), Co (99.95 %), Ni (99.98 %), and Nb (99.95 %) [56,57]. Element masses were measured such that a compositional threshold of 0.1 at.% was maintained for each sample batch. Alloying was performed using an Edmund Bühler GmbH 200AM arc melter using a Ti-gettered 99.998 % argon atmosphere, at a pressure of 0.7 bar, and a water-cooled copper hearth. Sample batches of weight 6 g and 12 g were homogenized by five successive melting and solidifying cycles inside the arc melter chamber. All BMG test specimen geometries (rods and bars) were produced using the suction casting facility integrated into the arc melter, wherein molten alloy was pulled by vacuum into a water-cooled copper mold cavity. Several different test specimen geometries were required to fulfil all of the required characterization. Test specimen geometries for compression testing, differential scanning calorimetry (DSC), and fatigue testing were ϕ 4 mm \times 4 mm cylinders, ϕ 3 mm \times 0.5 mm discs, and 3 mm \times 3 mm \times 30 mm bars, respectively. BMG rods measuring ϕ 5 mm \times 45 mm were suction cast from the 12 g sample buttons to facilitate the compression test specimens, BMG rods measuring ϕ 3 mm \times 32 mm were cast from the 6 g sample buttons to facilitate the DSC test specimens, and rectangular bars measuring 3.5 mm \times 3.5 mm \times 30 mm were cast from the 6 g sample buttons to facilitate the fatigue test specimens. Amorphicity for each as-cast part was confirmed by X-ray diffraction (XRD). The top and bottom circular faces of the suction cast BMG rods were scanned. A single scan was performed at the center of one of the four larger rectangular faces on the rectangular bars. XRD was performed using a Siemens D500 X-ray Diffractometer, incorporating a copper target (Cu-K_α , $\lambda = 1.5406 \text{ \AA}$), set at 40 kV and 30 mA. A 20 scan range from 20° to 90° was used in conjunction with a maximum step size of $0.08^\circ/\text{step}$ and a dwell time of 1.0 s/step. Samples were assumed fully amorphous if no crystalline peaks were recorded during the XRD scan cycle(s). Finally, compositions were also qualitatively validated using EDS performed on a Hitachi Regulus 8230 Ultra-high-resolution SEM fitted with an Oxford Instruments Ultim Max 170 EDS Detector.

2.2. Compression testing of BMG alloys

Compression test specimens were machined from ϕ 5 \times 45 mm BMG rods. Each end of the ϕ 5 mm rod was turned to finished dimensions ϕ 4 mm \times 10.5 mm using an Iscar PVD TiAlN + TiN coated CCMT 09 T304-SM turning insert with a tip radius of 0.3 mm, under flood coolant. Cutting conditions used were a nominal cutting speed of $0.183 \pm 0.017 \text{ m/s}$ and a feed per revolution of 0.07 mm. Two cylinders measuring ϕ 4 mm \times 4.5 mm were sectioned from both of the machined ends producing four compression test specimens per BMG rod. Sectioning was performed using a Buehler IsoMet1000 precision saw fitted with a Buehler ϕ 127 mm \times 0.4 mm 15HC diamond wafering blade. A cutting speed of 800 rpm and a load of 200 g were used during sectioning. The ends of each ϕ 4 mm \times 4.5 mm cylinder were ground to finished height of 4 mm with a nominal surface roughness of $\text{Ra} \sim 1 \mu\text{m}$ using standard P1200 grit SiC abrasive paper. Finished test specimen dimensions were measured at ϕ 3.96 mm \pm 0.07 mm \times 4.05 \pm 0.41 mm.

Compression testing was performed on a Hounsfield H50KS universal tester fitted with a Maywood Instruments U4000S 50

kN s-type load cell. A matched set of 20 mm precision ground, hardened tool-steel compression platens, comprising a fixed lower platen and a flexible upper platen attached to the crosshead. No lubrication or frictionless surface coatings were used during testing. Two strain-rates of 0.003 min^{-1} and 0.005 min^{-1} were used, from which the crosshead speed was determined based on the actual test specimen geometry. Testing machine compliance was characterized prior to compression testing so as to isolate its influence on the encoder-recorded strain.

2.3. Differential scanning calorimetry (DSC) of BMG alloys

DSC test specimens were precision sawn from ϕ 3 mm \times 32 mm suction cast BMG rods, producing ~ 21 , ϕ 3 mm \times 0.56 mm, test specimens per rod. BMG discs were thereafter ground to achieve the required test specimen mass of 28 mg. All test specimens were cleaned with acetone prior to DSC testing. A Stanton Redcroft STA1500 high temperature DSC and a low temperature Netzsch Polyma 214 were used to perform DSC scanning of test specimens; the high temperature DSC was used to perform constant heating experiments at $20 \text{ }^\circ\text{C}\cdot\text{min}^{-1}$ up to $1000 \text{ }^\circ\text{C}$, and the low temperature DSC used to perform isothermal holding experiments up to $600 \text{ }^\circ\text{C}$. Test specimens were halved from 28 mg to 14 mg for use in the Netzsch Polyma 214 to prevent any potential exothermal damage to the sensing equipment. All DSC scans were performed in a flowing nitrogen atmosphere. Open-top ϕ 5.5 mm \times 4 mm Pt-Rh crucibles were used in the STA1500 and ϕ 6 mm \times 40 μl aluminum pierced-lid crucibles were used in the Netzsch Polyma 214. Isothermal holding temperatures were determined based on the results of the constant heating experiments wherein the glass transition temperature, T_g , and the crystallization temperature, T_x , were measured. Several isothermal scans were performed on each composition. In each case, a heating rate of $20 \text{ }^\circ\text{C}\cdot\text{min}^{-1}$ was used to reach the selected isothermal hold temperature.

2.4. Fatigue testing of BMG alloys

Fatigue test specimens were ground square suction-cast BMG bars. Finished dimension were 3 mm \times 3 mm \times 30 mm. Test specimen geometry and fatigue testing conditions were selected to be comparable to similar fatigue studies of BMG materials presented in the literature [31,58–60]. All test specimens were ground up to P1200 grit with the grinding direction along the length of the bar. Fatigue testing was performed using the 4-point bend test (4PBT) configuration on a Dyna-Mess TE 7 HCF 4-column testing machine. A support span of 20 mm and loading span of 10 mm was used in conjunction with ϕ 6 mm or ϕ 5 mm hardened tools steel rollers. The arrangement of the 4PBT spans relative to the BMG fatigue test specimen is shown in Fig. 1 (a), along with an example of a BMG fatigue test specimen, Fig. 1 (b). Test specimens were not pre-cracked.

Four stress ranges ($\Delta\sigma$), 1000 MPa, 600 MPa, 400 MPa, and 200 MPa, were selected as the fatigue testing conditions. The full list of fatigue testing parameters used throughout testing is provided in Table 1. Testing inputs for software required a mid-load, F_{mid} (N), a force amplitude, F_a (N), a force ramp rate to reach the mid-load, F ($\text{N}\cdot\text{s}^{-1}$), an optional fade-in duration, N_{fade} (cycles), a test frequency, f_z (Hz), and an oscillation waveform, which, for this work, was sinusoidal. From the specified stress ranges, the values of for each of the loading forces, F , was calculated using Eqn. (1):

$$\sigma = \frac{3F(S_2 - S_1)}{2BH^2} \quad (1)$$

where B is the sample breadth, H the sample height, S_2 the support span width, and S_1 (mm) the loading span width. Parameter values are listed in Table 1. Loading forces determined using Eqn. (1) were

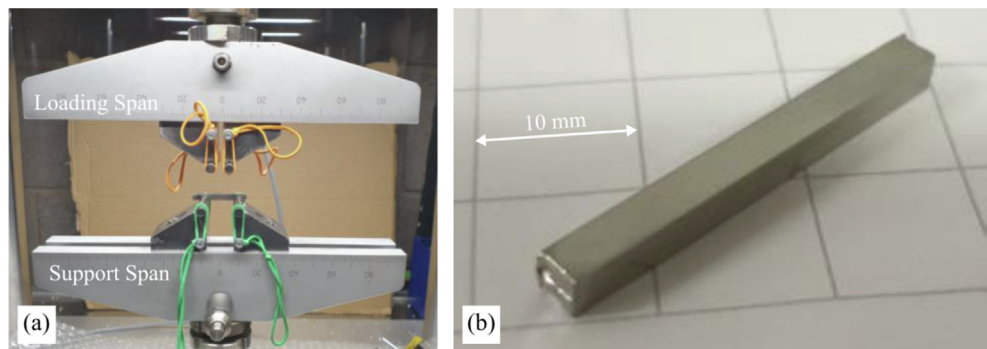


Fig. 1. (a) 4PBT fatigue testing configuration with BMG test specimen position on the loading span rollers. (b). 3 mm × 3 mm × 30 mm BMG fatigue test specimen.

Table 1

BMG 4PBT fatigue testing experiment inputs for the four selected stress ranges, $\Delta\sigma$ [MPa].

| Parameter | Description | Units | Stress Range 1000 MPa | Stress Range 600 MPa | Stress Range 400 MPa | Stress Range 200 MPa |
|-------------------|--------------------------|----------|-----------------------|----------------------|----------------------|----------------------|
| S_1 | Loading Span | [mm] | 10 | 10 | 10 | 10 |
| S_2 | Support Span | [mm] | 20 | 20 | 20 | 20 |
| d_r | Roller Diameter | [mm] | 6 | 6 | 5 | 5 |
| B | Test Specimen Breadth | [mm] | 3 | 3 | 3 | 3 |
| H | Test Specimen Height | [mm] | 3 | 3 | 3 | 3 |
| F_{mid} | Mid Force | [N] | 1100 | 660 | 440 | 220 |
| F | Force Ramp Rate | [N/s] | 1–10 | 5 | 5–6 | 5–6 |
| F_a | Force Amplitude | [N] | 900 | 540 | 360 | 180 |
| F_z | Cyclic Frequency | [Hz] | 25 | 25 | 25 | 25 |
| N_{fade} | Number of Fade-in Cycles | [Cycles] | 10–125 | 25 | 25 | 25 |
| N_{max} | Max Number of Cycles | [Cycles] | 5×10^5 | 5×10^5 | 5×10^5 | 5×10^5 |
| – | Waveform | – | Sinewave | Sinewave | Sinewave | Sinewave |

calculated based on nominal sample dimensions. The actual sample dimensions were recorded prior to loading into the 4PBT enclosure, and the actual stress thereafter recalculated for each individual test specimen. The force ramp rate, F , was determined based on maintaining a strain rate, $\dot{\varepsilon}$, of the order of $1.0 \times 10^{-4} \text{ s}^{-1}$, using Eqn. (2):

$$\dot{\varepsilon} = \frac{6H\nu}{S_2^2} \quad (2)$$

where ν is the crosshead speed ($\text{mm}\cdot\text{s}^{-1}$), and the remaining parameters are those listed in Table 1. As the crosshead speed is governed by the force ramp rate, ν in Eqn. (2) was calculated using Eqn. (3):

$$\nu = \frac{11FS_2^3}{32EBH^3} \quad (3)$$

where E is the elastic modulus (determined by compression testing), and the remaining parameters are those listed in Table 1. In total, 25 high cycle ($>10^4$ cycles) fatigue test experiments were performed on BMG test specimens made from each of the four compositions.

For comparison, and to mitigate the influence of test specimen geometry, several fatigue test specimens were manufactured from commercially available metals commonly used in the space industry. These were AISI 303 stainless steel (cold worked), AISI 304 stainless steel (cold worked) and Ti-6Al-4 V ELI. These alloys are commonly used in similar applications to those of interest in this work, i.e., anti-backlash gears (stainless steels) and flexure-based mechanisms (titanium alloys). The geometries and finishing processes used to create the test specimens were the same as those used for the BMG specimens, i.e., 3 mm × 3 mm × 30 mm, with a fine-ground surface finish.

3. Results

3.1. Compression testing of BMG alloys

Stress-strain plots for each of the four compositions, $Zr_{53}Al_{16-23.25}Ag_{7.75}$, $Zr_{49}Ti_{1.96}Cu_{37.24}Al_{9.8}Y_2$, $Zr_{60}Ti_2Nb_2Al_{7.5}Ni_{10}Cu_{18.5}$, and $Cu_{47}Zr_{46}Al_5Y_2$ (all composition values in at.% unless otherwise stated), are shown in Fig. 2 (a), (b), (c), and (d), respectively. Stress-strain responses were calculated from compliance-corrected force-extension compression test data. Along the abscissa in each sub-figure, relative strain is indicated by the 1 % scale bar. Each curve is offset by an arbitrary amount to maintain spacing between each of the six compression test datasets, labelled (i) to (vi). Stress data for each compression test is shown in the range 0.5 GPa to 2.5 GPa. Stresses below 0.5 GPa exhibited significant non-linearity due to machine compliance. A fit of the linear elastic region of each curve was extended to zero stress-strain for each dataset. The location of the yield stress (σ_y), where apparent, and the failure stress (σ_f) are indicated by an \times . The linear elastic response of the test specimen extends up to σ_y , and the region of plastic deformation between σ_y and σ_f . In all cases, test specimens failed catastrophically once the calculated stress reached σ_f . The corresponding test data from the 24 compression tests shown in Fig. 2 is provided in Table 2. The sample batch identification for each compression test specimen is given in column 4, where the alphanumeric groupings correspond to the composition label, original sample mass, sample production sequence, BMG rod production sequence, and compression test specimen ID, respectively. As indicated, two different sample batches were used to produce the rod feedstock used to make the test specimens for each composition. Cylindrical test specimen dimensions measured prior to compression testing, applied strain-rate, and published elastic modulus for each of the compositions investigated are given in columns 5, 6, and 7, respectively. Two different strain rates, 0.003 min^{-1} and 0.005 min^{-1}

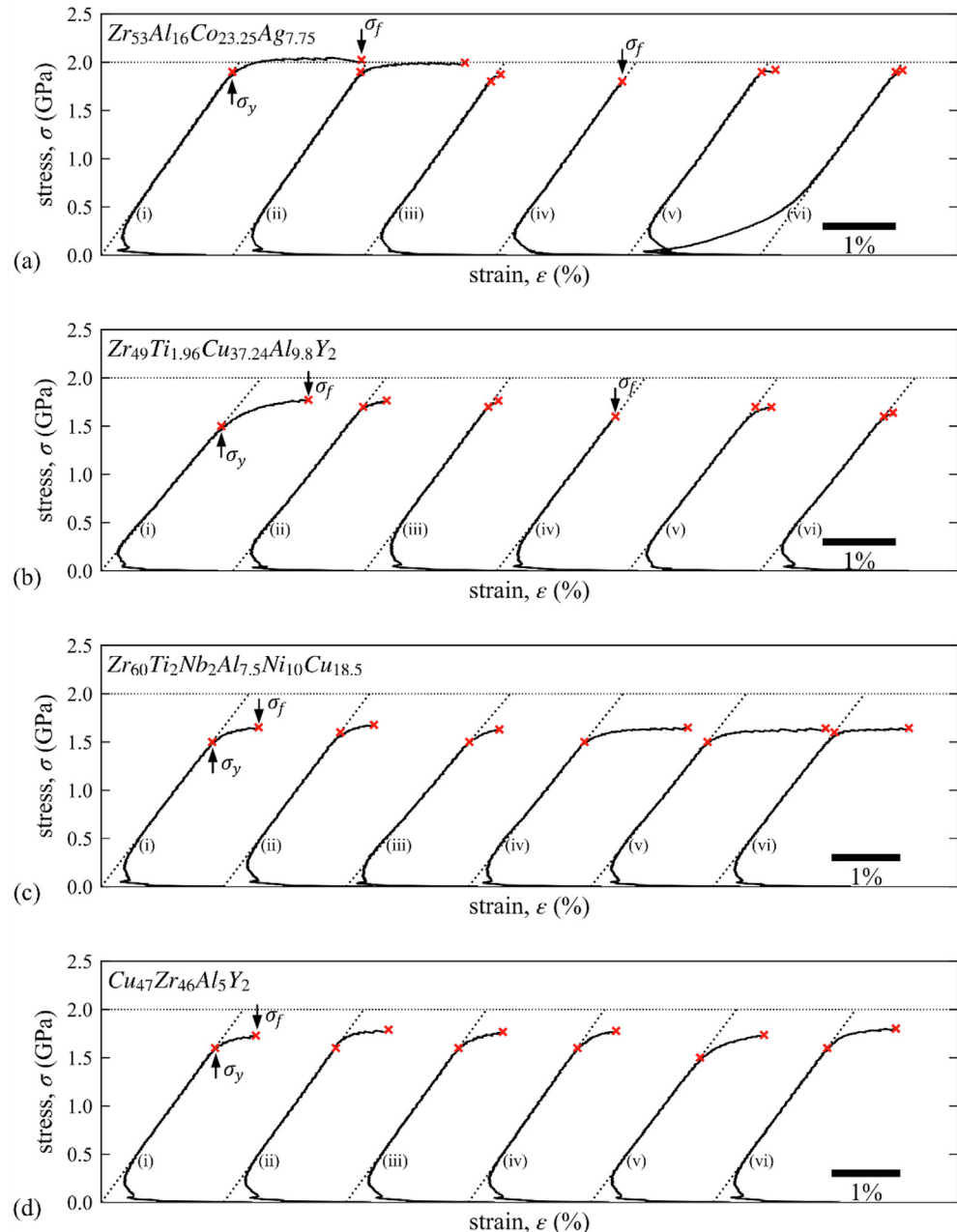


Fig. 2. Compression test results showing $\sigma(\epsilon)$ plots of six compression test specimens for each composition. (a) $Zr_{53}Al_{16}Co_{23.25}Ag_{7.75}$ (at.%), (b) $Zr_{49}Ti_{1.96}Cu_{37.24}Al_{9.8}Y_2$ (at.%), (c) $Zr_{60}Ti_2Nb_2Al_{7.5}Ni_{10}Cu_{18.5}$ (at.%), and (d) $Cu_{47}Zr_{46}Al_5Y_2$ (at.%). Scale bar on each sub-image represents a strain of 1%. Yield stress (σ_y), where apparent, and/or failure stress (σ_f) indicated in sequence on each trace (i-vi). Non-linearity in the stress-strain data below 0.5 GPa was due to compression testing machine compliance.

were used during testing (column 6). Columns 11 and 12, giving the measured values for σ_y and σ_f correspond to the \times location shown in Fig. 2, along with the corresponding elastic (ϵ_e), plastic (ϵ_p), and total strains (ϵ_{max}) for specimen. Photographs of typical destroyed testing specimens for all four compositions are shown in Fig. 3. Regardless of test conditions or recorded stress-strain response, test specimens from each of the four compositions failed in the manner indicated in Fig. 3. $Zr_{53}Al_{16}Co_{23.25}Ag_{7.75}$ (Fig. 3 (a)) shattered into a significant number of millimeter-sized or smaller fragments. $Zr_{49}Ti_{1.96}Cu_{37.24}Al_{9.8}Y_2$ failed in a similar manner (Fig. 3 (b)), however the fragments were typically larger than those shown in (Fig. 3 (a)). Test specimens produced from $Zr_{60}Ti_2Nb_2Al_{7.5}Ni_{10}Cu_{18.5}$ always fragmented into two pieces along a diagonal inclined approximately 45° from the cylindrical faces (Fig. 3 (c)).

Finally, $Cu_{47}Zr_{46}Al_5Y_2$ test specimens failed in a manner combining the characteristics of both $Zr_{49}Ti_{1.96}Cu_{37.24}Al_{9.8}Y_2$ (Fig. 3 (b)) and $Zr_{60}Ti_2Nb_2Al_{7.5}Ni_{10}Cu_{18.5}$ (Fig. 3 (c)), in that the debris comprised several larger masses exhibiting the 45° failure plane and several smaller fragments ejected from the larger pieces. An enlarged view of the fracture surface of a $Zr_{60}Ti_2Nb_2Al_{7.5}Ni_{10}Cu_{18.5}$ compression test specimen is shown in Fig. 3 (e). Apparent on the fracture surfaces are smooth striations aligned with the shearing direction. The same test specimen reassembled is shown in Fig. 3 (f), further illustrating the orientation of the plane of failure. The damage apparent to the lower left and top right edges of the test specimen shown in Fig. 3 (f) was caused by the compression platens at the time of failure. Finally, the summarized compression testing results obtained for each of the four compositions investigated are given in Table 3.

Table 2

Extracted data from $F(x)$ (not shown) and $\sigma(\varepsilon)$ plots produced from compression testing using cylindrical sample dimensions, diameter (D) \times length (L) and applied strain-rates, $\dot{\varepsilon}$. $E_{\text{pub.}}$ is the published elastic modulus for the composition, $E_{\text{expt.}}$ is the elastic modulus determined in this work, F_{max} is the maximum force recorded during compression testing, x_{max} is the maximum corrected extension recorded during compression testing, σ_y is the yield stress, σ_f is the fracture/failure stress, ε_e is the elastic strain limit, ε_p is the plastic strain limit, and ε_{max} is the maximum strain.

| # | Fig. 2 | Composition (at.%) | Batch ID | $D \times L$ | $\dot{\varepsilon}$ | $E_{\text{pub.}}$ | $E_{\text{expt.}}$ | F_{max} | x_{max} | σ_y | σ_f | ε_e | ε_p | ε_{max} |
|----|---------|--|------------------|--------------------|---------------------|-------------------|--------------------|------------------|------------------|------------|------------|-----------------|-----------------|----------------------------|
| | | | | [mm] | [min $^{-1}$] | [N/mm 2] | [N/mm 2] | [kN] | [mm] | [GPa] | [GPa] | [%] | [%] | [%] |
| 1 | (a-i) | Zr ₅₃ Al ₁₆ Co _{23.25} Ag _{7.75} | C12-12G-004-R1-A | 3.97 \times 3.99 | 0.005 | 94,000 | 95442.2 | 25.4 | 0.158 | 1.9 | 2.0 | 2.0 | 2.0 | 4.0 |
| 2 | (a-ii) | Zr ₅₃ Al ₁₆ Co _{23.25} Ag _{7.75} | C12-12G-004-R1-B | 3.96 \times 4.10 | 0.005 | 94,000 | 98257.3 | 24.6 | 0.144 | 1.9 | 2.0 | 1.9 | 1.6 | 3.5 |
| 3 | (a-iii) | Zr ₅₃ Al ₁₆ Co _{23.25} Ag _{7.75} | C12-24G-003-R2-A | 3.97 \times 4.05 | 0.003 | 94,000 | 93944.6 | 23.2 | 0.084 | 1.8 | 1.9 | 1.9 | 0.2 | 2.1 |
| 4 | (a-iv) | Zr ₅₃ Al ₁₆ Co _{23.25} Ag _{7.75} | C12-24G-003-R2-B | 3.97 \times 4.14 | 0.005 | 94,000 | 94444.9 | 21.9 | 0.078 | – | 1.8 | 1.9 | 0.0 | 1.9 |
| 5 | (a-v) | Zr ₅₃ Al ₁₆ Co _{23.25} Ag _{7.75} | C12-24G-003-R2-C | 3.90 \times 4.31 | 0.003 | 94,000 | 93807.3 | 22.9 | 0.096 | 1.9 | 1.9 | 2.0 | 0.2 | 2.2 |
| 6 | (a-vi) | Zr ₅₃ Al ₁₆ Co _{23.25} Ag _{7.75} | C12-24G-003-R2-D | 3.91 \times 4.04 | 0.003 | 94,000 | 88303.1 | 23.0 | 0.090 | 1.9 | 1.9 | 2.1 | 0.1 | 2.2 |
| 7 | (b-i) | Zr ₄₉ Ti _{1.96} Cu _{37.24} Al _{9.8} Y ₂ | C16-12G-004-R1-B | 4.05 \times 3.91 | 0.005 | 86,000 | 82296.2 | 22.8 | 0.123 | 1.5 | 1.8 | 1.8 | 1.3 | 3.1 |
| 8 | (b-ii) | Zr ₄₉ Ti _{1.96} Cu _{37.24} Al _{9.8} Y ₂ | C16-12G-004-R1-C | 3.94 \times 4.04 | 0.005 | 86,000 | 86056.3 | 21.5 | 0.094 | 1.7 | 1.8 | 2.0 | 0.3 | 2.3 |
| 9 | (b-iii) | Zr ₄₉ Ti _{1.96} Cu _{37.24} Al _{9.8} Y ₂ | C16-24G-002-R1-C | 3.93 \times 4.00 | 0.003 | 86,000 | 90646.7 | 21.4 | 0.081 | 1.7 | 1.8 | 1.9 | 0.1 | 2.0 |
| 10 | (b-iv) | Zr ₄₉ Ti _{1.96} Cu _{37.24} Al _{9.8} Y ₂ | C16-24G-002-R1-D | 4.00 \times 3.95 | 0.005 | 86,000 | 88627.9 | 19.5 | 0.069 | – | 1.6 | 1.7 | 0.0 | 1.7 |
| 11 | (b-v) | Zr ₄₉ Ti _{1.96} Cu _{37.24} Al _{9.8} Y ₂ | C16-24G-002-R2-A | 4.02 \times 4.45 | 0.003 | 86,000 | 88150.4 | 21.6 | 0.097 | 1.7 | 1.7 | 1.8 | 0.4 | 2.2 |
| 12 | (b-vi) | Zr ₄₉ Ti _{1.96} Cu _{37.24} Al _{9.8} Y ₂ | C16-24G-002-R2-B | 3.94 \times 4.15 | 0.003 | 86,000 | 85177.4 | 20.0 | 0.084 | 1.6 | 1.6 | 1.9 | 0.1 | 2.0 |
| 13 | (c-i) | Zr ₆₀ Ti ₂ Nb ₂ Al _{7.5} Ni ₁₀ Cu _{18.5} | C18-12G-003-R1-A | 3.88 \times 4.39 | 0.003 | 81,000 | 82728.3 | 19.5 | 0.113 | 1.5 | 1.7 | 1.8 | 0.8 | 2.6 |
| 14 | (c-ii) | Zr ₆₀ Ti ₂ Nb ₂ Al _{7.5} Ni ₁₀ Cu _{18.5} | C18-12G-003-R1-B | 3.92 \times 4.02 | 0.003 | 81,000 | 83893.5 | 20.2 | 0.099 | 1.6 | 1.7 | 1.9 | 0.6 | 2.5 |
| 15 | (c-iii) | Zr ₆₀ Ti ₂ Nb ₂ Al _{7.5} Ni ₁₀ Cu _{18.5} | C18-12G-004-R1-A | 3.93 \times 3.95 | 0.005 | 81,000 | 74421.2 | 19.8 | 0.099 | 1.5 | 1.6 | 2.0 | 0.5 | 2.5 |
| 16 | (c-iv) | Zr ₆₀ Ti ₂ Nb ₂ Al _{7.5} Ni ₁₀ Cu _{18.5} | C18-12G-004-R1-B | 3.90 \times 3.96 | 0.005 | 81,000 | 79034.6 | 19.7 | 0.142 | 1.5 | 1.6 | 1.9 | 1.7 | 3.6 |
| 17 | (c-v) | Zr ₆₀ Ti ₂ Nb ₂ Al _{7.5} Ni ₁₀ Cu _{18.5} | C18-12G-004-R1-C | 3.94 \times 3.95 | 0.005 | 81,000 | 78594.0 | 20.0 | 0.152 | 1.5 | 1.6 | 1.9 | 1.9 | 3.8 |
| 18 | (c-vi) | Zr ₆₀ Ti ₂ Nb ₂ Al _{7.5} Ni ₁₀ Cu _{18.5} | C18-12G-004-R1-D | 4.00 \times 4.03 | 0.003 | 81,000 | 80657.6 | 20.7 | 0.129 | 1.6 | 1.6 | 1.9 | 1.3 | 3.2 |
| 19 | (d-i) | Cu ₄₇ Zr ₄₆ Al ₅ Y ₂ | C35-12G-004-R1-A | 3.92 \times 4.01 | 0.005 | 75,000 | 85999.6 | 20.9 | 0.101 | 1.6 | 1.7 | 1.9 | 0.6 | 2.5 |
| 20 | (d-ii) | Cu ₄₇ Zr ₄₆ Al ₅ Y ₂ | C35-12G-004-R1-B | 3.98 \times 4.02 | 0.005 | 75,000 | 87251.6 | 22.3 | 0.109 | 1.6 | 1.8 | 1.9 | 0.8 | 2.7 |
| 21 | (d-iii) | Cu ₄₇ Zr ₄₆ Al ₅ Y ₂ | C35-12G-004-R1-C | 3.93 \times 4.04 | 0.005 | 75,000 | 86969.8 | 21.4 | 0.104 | 1.6 | 1.8 | 1.9 | 0.7 | 2.6 |
| 22 | (d-iv) | Cu ₄₇ Zr ₄₆ Al ₅ Y ₂ | C35-24G-003-R1-A | 4.04 \times 4.01 | 0.003 | 75,000 | 89863.0 | 22.8 | 0.097 | 1.6 | 1.8 | 1.8 | 0.6 | 2.4 |
| 23 | (d-v) | Cu ₄₇ Zr ₄₆ Al ₅ Y ₂ | C35-24G-003-R1-B | 3.95 \times 4.00 | 0.003 | 75,000 | 83892.1 | 21.3 | 0.114 | 1.5 | 1.7 | 1.8 | 1.0 | 2.8 |
| 24 | (d-vi) | Cu ₄₇ Zr ₄₆ Al ₅ Y ₂ | C35-24G-003-R2-A | 3.90 \times 3.96 | 0.003 | 75,000 | 85734.7 | 21.5 | 0.118 | 1.7 | 1.8 | 2.0 | 1.0 | 3.0 |

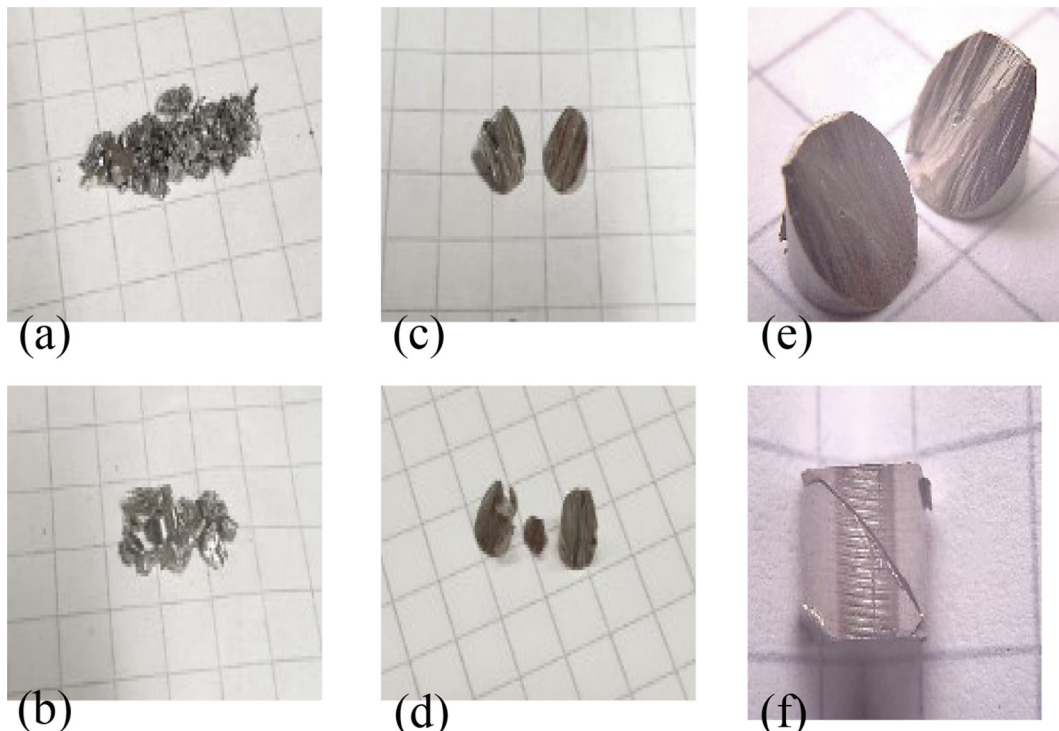


Fig. 3. Typical fracturing morphologies observed for test specimens of each of the four project compositions. (a) Zr₅₃Al₁₆Co_{23.25}Ag_{7.75} (at.%), (b) Zr₄₉Ti_{1.96}Cu_{37.24}Al_{9.8}Y₂ (at.%), (c) Zr₆₀Ti₂Nb₂Al_{7.5}Ni₁₀Cu_{18.5} (at.%), and (d) Cu₄₇Zr₄₆Al₅Y₂ (at.%). (e) Magnified view of fracture surface of specimen Fig. 3 (c) showing fracture surface along the $\sim 45^\circ$ plane. (f) Reassembled halves of the fractured test specimen, Fig. 3 (c), further illustrating the $\sim 45^\circ$ fracture plane.

indicating the calculated average elastic modulus (E), yield stress (σ_y), failure stress (σ_f), elastic strain (ε_e), and plastic strain (ε_p), respectively.

3.2. Differential scanning calorimetry (DSC) of BMG alloys

Fig. 4 shows the results of the constant heating DSC scans performed, using the Stanton Redcroft STA1500, on test specimens from all four compositions. Tests were performed at a constant rate of $20\text{ }^\circ\text{C}\cdot\text{min}^{-1}$ starting from room temperature ($\sim 20\text{ }^\circ\text{C}$). Four

Table 3

Experimentally determined mechanical properties for each composition. Values provided represent the average (μ) and one standard deviation (σ) across all test specimens for each composition using the data obtained in Table 2.

| Composition (at.%) | E [GPa] | σ_y [GPa] | σ_f [GPa] | ε_e [%] | ε_p [%] |
|--|-----------|------------------|------------------|---------------------|---------------------|
| Zr ₅₃ Al ₁₆ Co _{23.25} Ag _{7.75} | 94 ± 3 | 1.9 ± 0.0 | 1.9 ± 0.1 | 2.0 ± 0.1 | 0.7 ± 0.9 |
| Zr ₄₉ Ti _{1.96} Cu _{37.24} Al _{9.8} Y ₂ | 87 ± 3 | 1.6 ± 0.1 | 1.7 ± 0.1 | 1.9 ± 0.1 | 0.4 ± 0.5 |
| Zr ₆₀ Ti ₂ Nb ₂ Al _{7.5} Ni ₁₀ Cu _{18.5} | 80 ± 3 | 1.5 ± 0.1 | 1.6 ± 0.1 | 1.8 ± 0.1 | 1.1 ± 0.6 |
| Cu ₄₇ Zr ₄₆ Al ₅ Y ₂ | 87 ± 2 | 1.6 ± 0.1 | 1.8 ± 0.1 | 1.9 ± 0.1 | 0.8 ± 0.2 |

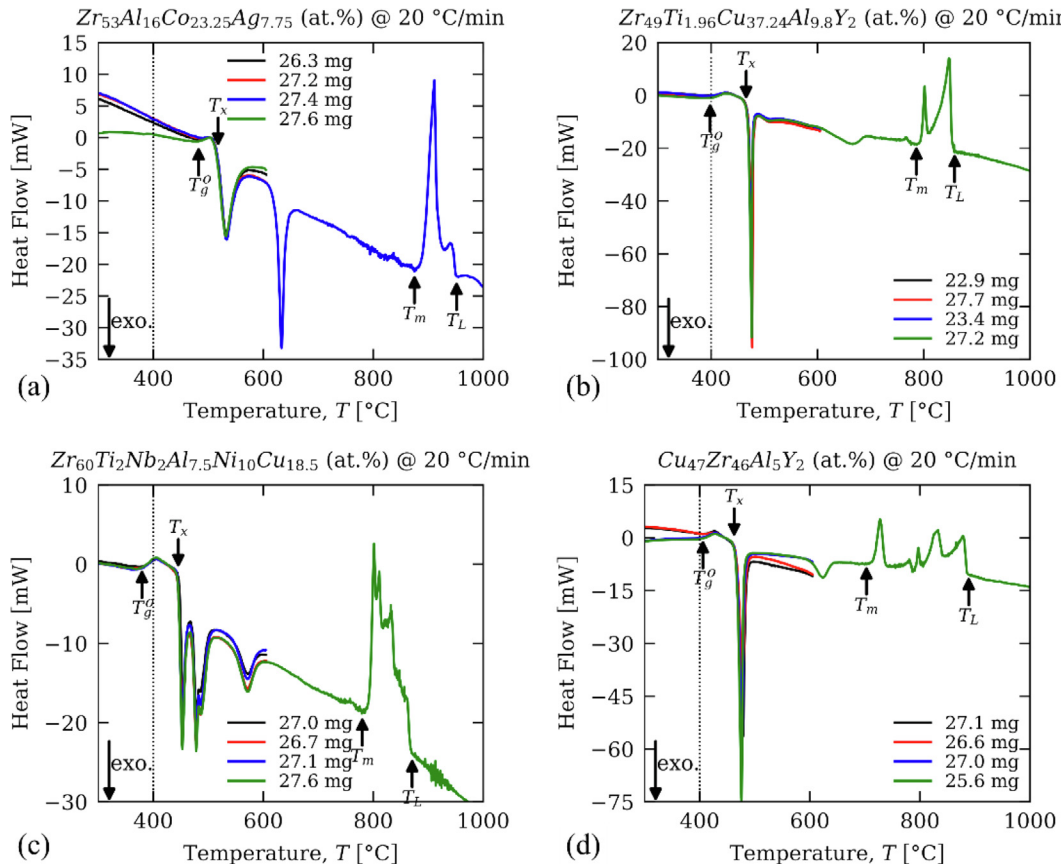


Fig. 4. Constant heating DSC scans performed on the STA1500 at 20 °C/min from ~20 °C to 1000 °C. Four scans per alloy: three up to 600 °C and one up to 1000 °C. (a) Zr₅₃Al₁₆Co_{23.25}Ag_{7.75} (at.%), (b) Zr₄₉Ti_{1.96}Cu_{37.24}Al_{9.8}Y₂ (at.%), (c) Zr₆₀Ti₂Nb₂Al_{7.5}Ni₁₀Cu_{18.5} (at.%), and (d) Cu₄₇Zr₄₆Al₅Y₂ (at.%). Onset glass transition temperature (T_g^o), crystallization temperature (T_x), melting temperature (T_m), and liquidus temperature (T_L). Exothermic reactions show as negatively biased heat flow.

scans were performed for each composition, three up to 600 °C and one up to 1000 °C. The dotted vertical line at 400 °C in each sub-figure highlights the selected maximum operating temperature for space-based mechanisms. Indicated on each curve is the location of the glass transition temperature, T_g , the crystallization onset temperature, T_x , the melting temperature, T_m , and the liquidus temperature, T_L . The test specimen mass in mg is indicated in the figure legends. Note, for the purposes of this work, the heat flow (mW) recorded by the apparatus is inconsequential; only the indicated transition temperatures are of interest from an operating range perspective. A more detailed view of a single DSC curve for each composition is provided in Fig. 5, showing values for onset and conclusion of the glass transition, and onset and peak crystallization temperatures. The vertical offset applied to each curve is arbitrary. Three of the four of the compositions exhibited T_g at or above the 400 °C threshold required for operation in the space environment, with only Zr₆₀Ti₂Nb₂Al_{7.5}Ni₁₀Cu_{18.5} exhibiting a T_g slightly below the threshold. With the most critical transition temperatures determined from constant heating scans, a range of isothermal DSC scans was performed to characterize the extent

of the supercooled liquid region between T_g and T_x traditionally illustrated on a Time-Temperature-Transformation (TTT) diagram. The results of the isothermal DSC scans performed on the Netzsch Polyma 214 DSC are shown in Figure A. 1 in the Appendix A. The results obtained from Figure A. 1, i.e., peak crystallization temperature and isothermal hold temperature, were then used to develop qualitative TTT diagrams, shown in Fig. 6. In each sub-figure, the peak crystallization temperature, T_x , and the onset glass transition temperature, T_g^o , are indicated by the dotted horizontal lines. The first data point (×) on the time axis is the measured peak crystallization temperature, T_x (peak), determined during constant heating experiments performed under the same conditions and using the same apparatus as the isothermal scans. The subsequent data points (●) are the peak crystallization times obtained from Figure A. 1 for a given isothermal holding temperature, T_{iso} . The results demonstrate the relative potential for thermoplastic-based processing of each alloy in the supercooled liquid region when $T_g < T < T_x$. Finally, a summary of thermal properties for each composition is provided in Table 4.

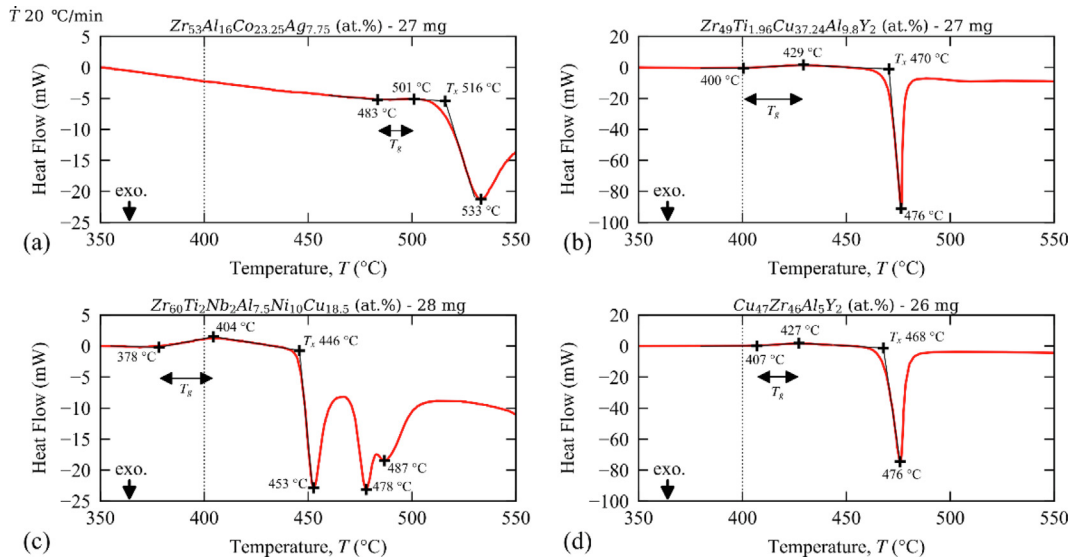


Fig. 5. Constant heating ($\dot{T} = 20^{\circ}\text{C}/\text{s}$) DSC scans performed on the STA1500 DSC. T_g : glass transition temperature range. T_x : crystallization onset. Test specimen masses indicated for each scan. (a) $\text{Zr}_{53}\text{Al}_{16}\text{Co}_{23.25}\text{Ag}_{7.75}$ (at.%), (b) $\text{Zr}_{49}\text{Ti}_{1.96}\text{Cu}_{37.24}\text{Al}_{9.8}\text{Y}_2$ (at.%), (c) $\text{Zr}_{60}\text{Ti}_2\text{Nb}_2\text{Al}_{7.5}\text{Ni}_{10}\text{Cu}_{18.5}$ (at.%), and (d) $\text{Cu}_{47}\text{Zr}_{46}\text{Al}_5\text{Y}_2$ (at.%).

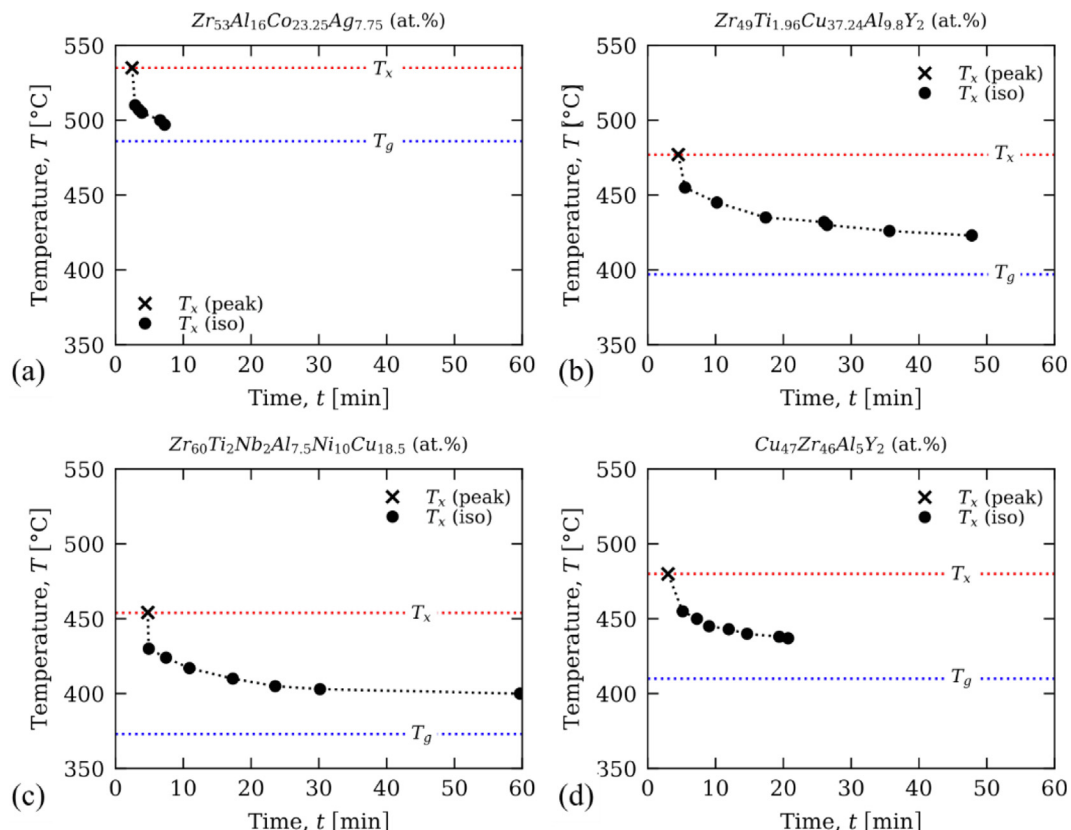


Fig. 6. Experimentally determined time-temperature-transformation for each of the project compositions. (a) $\text{Zr}_{53}\text{Al}_{16}\text{Co}_{23.25}\text{Ag}_{7.75}$ (at.%), (b) $\text{Zr}_{49}\text{Ti}_{1.96}\text{Cu}_{37.24}\text{Al}_{9.8}\text{Y}_2$ (at.%), (c) $\text{Zr}_{60}\text{Ti}_2\text{Nb}_2\text{Al}_{7.5}\text{Ni}_{10}\text{Cu}_{18.5}$ (at.%), and (d) $\text{Cu}_{47}\text{Zr}_{46}\text{Al}_5\text{Y}_2$ (at.%). (●) crystallization peak location data points extracted from Figure A. 1. (×) crystallization peak time recorded during the constant heating experiments from Fig. 5.

3.3. Fatigue testing of BMG alloys

Four-point-bend (4 PB) fatigue tests were performed on the BMG alloys under investigation. A complete list of the testing parameters used (summarized in Table 1) for all 25 fatigue tests performed is given in Table B. 1 in Appendix B. The corresponding results of the fatigue testing experiments listed in Table B. 1 are

provided in Table 5. The traditional Wöhler plots of the extracted S–N data (column 5 and column 8, respectively, Table B. 1) for all compositions are shown in Fig. 7, where stress range, $\Delta\sigma$, is plotted against maximum number of cycles, N_{\max} . The arrows attached to markers in each sub-figure identify S–N values where the test specimen did not fail before reaching the maximum number of cycles specified.

Table 4

Experimentally determined temperature transitions for each of the project compositions. T_g : glass transition temperature; T_x : crystallization temperature; ΔT_x is extent of the supercooled liquid region (SCLR); T_m : melting temperature; T_L : liquidus temperature.

| Composition (at.%) | Onset T_g [°C] | End T_g [°C] | T_x [°C] | SCLR ΔT_x [°C] | T_m [°C] | T_L [°C] |
|--|------------------|----------------|------------|------------------------|------------|------------|
| Zr ₅₃ Al ₁₆ Co _{23.25} Ag _{7.75} | 483 | 501 | 516 | 33 | 875 | 954 |
| Zr ₄₉ Ti _{1.96} Cu _{37.24} Al _{9.8} Y ₂ | 400 | 429 | 470 | 70 | 787 | 858 |
| Zr ₆₀ Ti ₂ Nb ₂ Al _{7.5} Ni ₁₀ Cu _{18.5} | 378 | 404 | 446 | 68 | 780 | 870 |
| Cu ₄₇ Zr ₄₆ Al ₅ Y ₂ | 407 | 427 | 468 | 61 | 704 | 889 |

Table 5

Results of 4 PB fatigue testing performed on the Dyna-Mess fatigue testing machine. † Test stopped after set number of cycles, test specimen inspected, test restarted and run until test specimen failure or N_{max} reached. → Testing stopped after set number of cycles without test specimen failure.

| # | Composition (at.%) | δ_{max} [mm] | δ_{min} [mm] | N_{max} | σ_{max} [MPa] | σ_{min} [MPa] | $\Delta\sigma$ [MPa] | $\Delta\sigma_{target}$ [MPa] | σ_a [MPa] |
|----|---|---------------------|---------------------|-----------|----------------------|----------------------|----------------------|-------------------------------|------------------|
| 1 | Zr ₅₃ Al ₁₆ Co _{23.25} Ag _{7.75} | — | — | 0 | — | — | — | — | — |
| 2 | Zr ₅₃ Al ₁₆ Co _{23.25} Ag _{7.75} | 0.53 | 0.29 | 12,532 | 598 | 60 | 539 | 600 | 269 |
| 3 | Zr ₅₃ Al ₁₆ Co _{23.25} Ag _{7.75} | 0.17 | 0.04 | 88,418 | 408 | 40 | 367 | 400 | 184 |
| 4 | Zr ₅₃ Al ₁₆ Co _{23.25} Ag _{7.75} | 0.19 | 0.05 | 12,211 | 405 | 40 | 365 | 400 | 183 |
| 5 | Zr ₅₃ Al ₁₆ Co _{23.25} Ag _{7.75} † | 0.12 | 0.04 | 100,000 | 213 | 21 | 191 | 200 | 96 |
| 6 | Zr ₅₃ Al ₁₆ Co _{23.25} Ag _{7.75} † | 0.12 | 0.03 | 100,000 | 212 | 21 | 191 | 200 | 95 |
| 7 | Zr ₄₉ Ti _{1.96} Cu _{37.24} Al _{9.8} Y ₂ | 0.54 | 0.53 | 0 | 574 | 521 | 53 | 1000 | 26 |
| 8 | Zr ₄₉ Ti _{1.96} Cu _{37.24} Al _{9.8} Y ₂ | 0.50 | 0.28 | 17,206 | 605 | 61 | 545 | 600 | 272 |
| 9 | Zr ₄₉ Ti _{1.96} Cu _{37.24} Al _{9.8} Y ₂ † | 0.29 | 0.13 | 143,938 | 401 | 40 | 362 | 400 | 181 |
| 10 | Zr ₄₉ Ti _{1.96} Cu _{37.24} Al _{9.8} Y ₂ † | 0.20 | 0.03 | 188 | 402 | 41 | 362 | 400 | 181 |
| 11 | Zr ₄₉ Ti _{1.96} Cu _{37.24} Al _{9.8} Y ₂ | 0.22 | 0.07 | 23,682 | 437 | 44 | 394 | 400 | 197 |
| 12 | Zr ₄₉ Ti _{1.96} Cu _{37.24} Al _{9.8} Y ₂ → | 0.21 | 0.07 | 100,000 | 428 | 43 | 385 | 400 | 193 |
| 13 | Zr ₆₀ Ti ₂ Nb ₂ Al _{7.5} Ni ₁₀ Cu _{18.5} | 0.59 | 0.22 | 5249 | 1049 | 104 | 945 | 1000 | 473 |
| 14 | Zr ₆₀ Ti ₂ Nb ₂ Al _{7.5} Ni ₁₀ Cu _{18.5} † | 0.65 | 0.29 | 5562 | 1065 | 107 | 958 | 1000 | 479 |
| 15 | Zr ₆₀ Ti ₂ Nb ₂ Al _{7.5} Ni ₁₀ Cu _{18.5} | 0.43 | 0.22 | 46,037 | 523 | 52 | 471 | 600 | 236 |
| 16 | Zr ₆₀ Ti ₂ Nb ₂ Al _{7.5} Ni ₁₀ Cu _{18.5} †→ | 0.20 | 0.04 | 500,113 | 406 | 41 | 365 | 400 | 183 |
| 17 | Zr ₆₀ Ti ₂ Nb ₂ Al _{7.5} Ni ₁₀ Cu _{18.5} † | 0.23 | 0.07 | 157,665 | 400 | 40 | 360 | 400 | 180 |
| 18 | Zr ₆₀ Ti ₂ Nb ₂ Al _{7.5} Ni ₁₀ Cu _{18.5} → | 0.20 | 0.04 | 100,000 | 433 | 43 | 389 | 400 | 195 |
| 19 | Zr ₆₀ Ti ₂ Nb ₂ Al _{7.5} Ni ₁₀ Cu _{18.5} → | 0.23 | 0.06 | 100,000 | 430 | 43 | 387 | 400 | 193 |
| 20 | Cu ₄₇ Zr ₄₆ Al ₅ Y ₂ | 0.56 | 0.20 | 481 | 896 | 90 | 806 | 1000 | 403 |
| 21 | Cu ₄₇ Zr ₄₆ Al ₅ Y ₂ | 0.39 | 0.17 | 82,550 | 558 | 56 | 502 | 600 | 251 |
| 22 | Cu ₄₇ Zr ₄₆ Al ₅ Y ₂ | 0.27 | 0.11 | 27,211 | 406 | 41 | 365 | 400 | 183 |
| 23 | Cu ₄₇ Zr ₄₆ Al ₅ Y ₂ | 0.25 | 0.08 | 499 | 405 | 41 | 364 | 400 | 182 |
| 24 | Cu ₄₇ Zr ₄₆ Al ₅ Y ₂ | 0.20 | 0.04 | 66,710 | 438 | 44 | 394 | 400 | 197 |
| 25 | Cu ₄₇ Zr ₄₆ Al ₅ Y ₂ → | 0.19 | 0.03 | 100,000 | 429 | 42 | 386 | 400 | 193 |

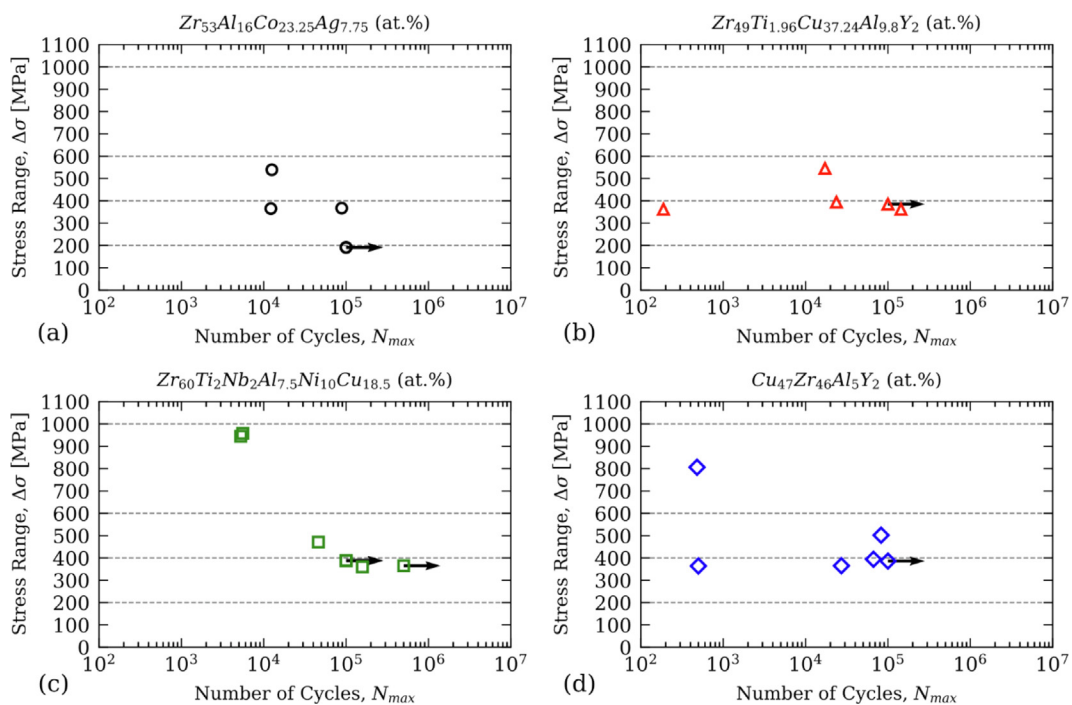


Fig. 7. S-N plots of fatigue test results listed in Table 5. (a) Zr₅₃Al₁₆Co_{23.25}Ag_{7.75} (at.%), (b) Zr₄₉Ti_{1.96}Cu_{37.24}Al_{9.8}Y₂ (at.%), (c) Zr₆₀Ti₂Nb₂Al_{7.5}Ni₁₀Cu_{18.5} (at.%), and (d) Cu₄₇Zr₄₆Al₅Y₂ (at.%). Arrows indicated test specimens that did not fail before reaching N_{max} . Horizontal dashed lines at σ_{target} . All other markers represent run-to-fail test specimens.

Examples of typical fatigue failure of test specimens from each composition are shown in Fig. 8 (a), (b), (c), and (d), for compositions $Zr_{53}Al_{16}Co_{23.25}Ag_{7.75}$, $Zr_{49}Ti_{1.96}Cu_{37.24}Al_{9.8}Y_2$, $Zr_{60}Ti_2Nb_2Al_{7.5}-Ni_{10}Cu_{18.5}$, and $Cu_{47}Zr_{46}Al_5Y_2$, respectively. The (i) column shows the test specimen reassembled and oriented such that the loading direction was vertically downwards in the figure window. The (ii) column shows the exposed fracture surface for each test specimen. Similar to what was observed during compression testing, $Zr_{53}Al_{16}-Co_{23.25}Ag_{7.75}$ fatigue test specimens typically fragmented into several pieces, $Zr_{49}Ti_{1.96}Cu_{37.24}Al_{9.8}Y_2$ into a smaller number of pieces, $Zr_{60}Ti_2Nb_2Al_{7.5}Ni_{10}Cu_{18.5}$ typically fractured into two pieces with a macroscopically jagged fracture surface, and $Cu_{47}Zr_{46}Al_5Y_2$ speci-

mens exhibited behavior between $Zr_{49}Ti_{1.96}Cu_{37.24}Al_{9.8}Y_2$ and $Zr_{60}-Ti_2Nb_2Al_{7.5}Ni_{10}Cu_{18.5}$, i.e., either fragmenting into several pieces or breaking in half, as shown in Fig. 8 (d). In the latter case, crack propagation observed was typically of the form shown in Fig. 8 (d-i), with the crack initially progressing vertically upwards then then changing direction once approximately halfway through the height of the cross-section and finally turning vertically upwards for final failure to the specimen. The fatigue testing apparatus control system was set to maintain the applied mid-load, F_{mid} , and load amplitude, F_a , during testing, so crack growth was captured by the encoder as an increase in the average displacement of the crosshead. For all $Zr_{53}Al_{16}Co_{23.25}Ag_{7.75}$, $Zr_{49}Ti_{1.96}Cu_{37.24}Al_{9.8}Y_2$,

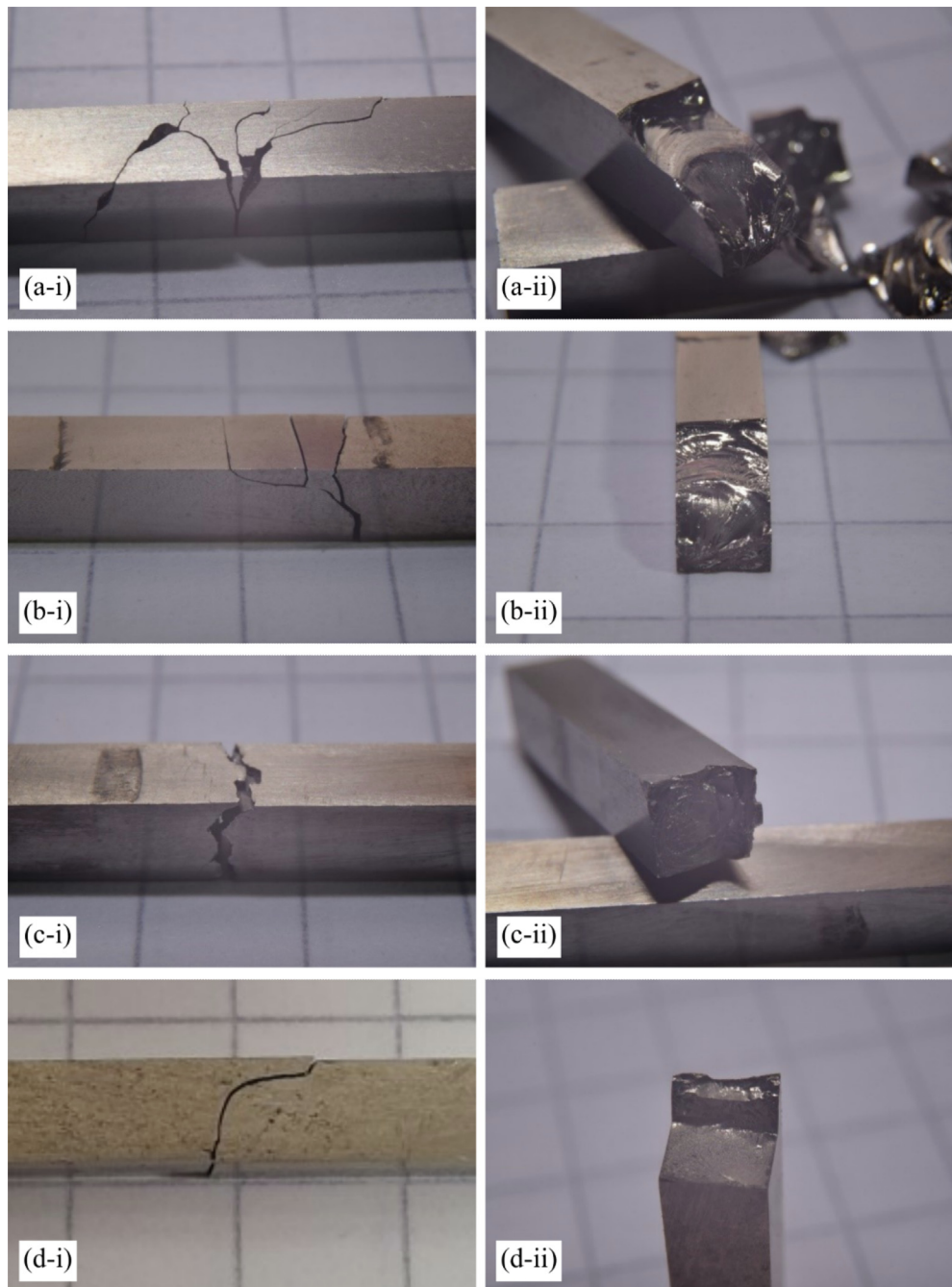


Fig. 8. Fracture types observed during fatigue testing. (a) $Zr_{53}Al_{16}Co_{23.25}Ag_{7.75}$ (at.%), (b) $Zr_{49}Ti_{1.96}Cu_{37.24}Al_{9.8}Y_2$ (at.%), (c) $Zr_{60}Ti_2Nb_2Al_{7.5}Ni_{10}Cu_{18.5}$ (at.%), and (d) $Cu_{47}Zr_{46}Al_5Y_2$ (at.%). Column (i) shows the reassembled test specimen with compression surface towards the top of the image and tension surface towards the bottom of the image in each case. Column (ii) shows the internal fracture surface for each test specimen.

and Cu₄₇Zr₄₆Al₅Y₂ test specimens, the time between crack formation and subsequent test specimen failure was typically less than one cycle. Catastrophic failure was energetic and resulted in fragments being distributed widely around the inside of the test chamber. Three Zr₆₀Ti₂Nb₂Al_{7.5}Ni₁₀Cu_{18.5} test specimens (rows 14, 15, and 17 in Table 5) exhibited significantly lower crack growth rates. Examination of the displacement vs cycle data from the fatigue testing software showed it took between 700 and 2000 cycles for the crack to propagate through the cross section of the specimen, i.e., a crack growth rate between 0.04 mm·s⁻¹ and 0.1 mm·s⁻¹, compared to $\gg 75$ mm·s⁻¹ for specimens that failed catastrophically. An example of one such specimen is shown in Fig. 9, corresponding to row 15 in Table 5. In this case, the crack propagation was slow enough that the test was stopped before the crack tip reached the top surface of the test specimen, Fig. 9 (a). On the tensile face of the specimen, the crack orientation is perpendicular to the side surfaces. The path of the crack through the height of the bar appears more tortuous. The images in Fig. 9 (b) show each side of the crack surfaces after the test specimen was mechanically separated. The crack surface exposed during the cyclic loading exhibits a smooth dull appearance, with the residual material exhibiting a rougher surface. SEM images taken of the same crack prior to separation are shown in Fig. 10. Fig. 10 (a) shows the entire crack length with regions of interest highlighted. Closer inspection of the crack, Fig. 10 (b), reveals the staircase morphology that developed during the crack propagation, i.e., as the crack progressed the growth direction flipped approximately between $\pm 45^\circ$ relative to the line of applied cyclic loading. Further detail of the individual steps comprising the crack are shown in Fig. 10 (c), along with evidence of shear bands emanating both normal and parallel to the step edge, as well as disconnected shear bands offset away from the crack. Shear banding was also observed to develop ahead of the crack tip, Fig. 10 (d).

Finally, the results of comparable fatigue testing performed on commercially available metal alloys (AISI 303, AISI 304, and Ti-6Al-4 V ELI) are shown in Fig. 11, along with those of BMG composition Zr₆₀Ti₂Nb₂Al_{7.5}Ni₁₀Cu_{18.5} (at.%), which exhibited the best fatigue performance of the four BMG compositions tested. The

dashed fit line in Fig. 11 indicates the nominal threshold for BMG performance under the testing conditions used in this work. Geometry and loading conditions for the commercial alloys were consistent with those used during fatigue testing of the BMG test specimens.

4. Discussion

BMG alloys have been shown to exhibit some of the most impressive mechanical properties of any metals with respect to strength, hardness, wear performance, oxidation resistance, elasticity, etc. [51,55,61,62]. Due to the amorphous nature of BMG alloys, additional processing capabilities are also possible in the form of thermoplastic forming, with injection molding, blow molding, extrusion-based additive manufacturing, and embossing all achieved [63–66]. Consequently, BMG alloys are of particular interest to the space industry, where high performance materials are required to operate under harsh conditions for extended periods.

4.1. Alloy selection and synthesis

The processing conditions developed to produce the alloys from pure elements using the arc melter were carefully controlled throughout. However, arc melter control is largely manual so there is significant potential for the operator to influence processing conditions unintentionally. Furthermore, mold filling during suction casting can influence the cooling rate experience by the casting volume at discrete locations. Changes in cooling rate can lead to atom-scale configurational changes in the amorphous matrix, potentially altering the thermomechanical properties.

4.2. BMG testing and performance

The mechanical testing performed as part of this work incorporated test specimens from several different sample batches, produced using ostensibly the same processing conditions. The most apparent influence of the influence of processing conditions on mechanical properties was significant disparity between speci-

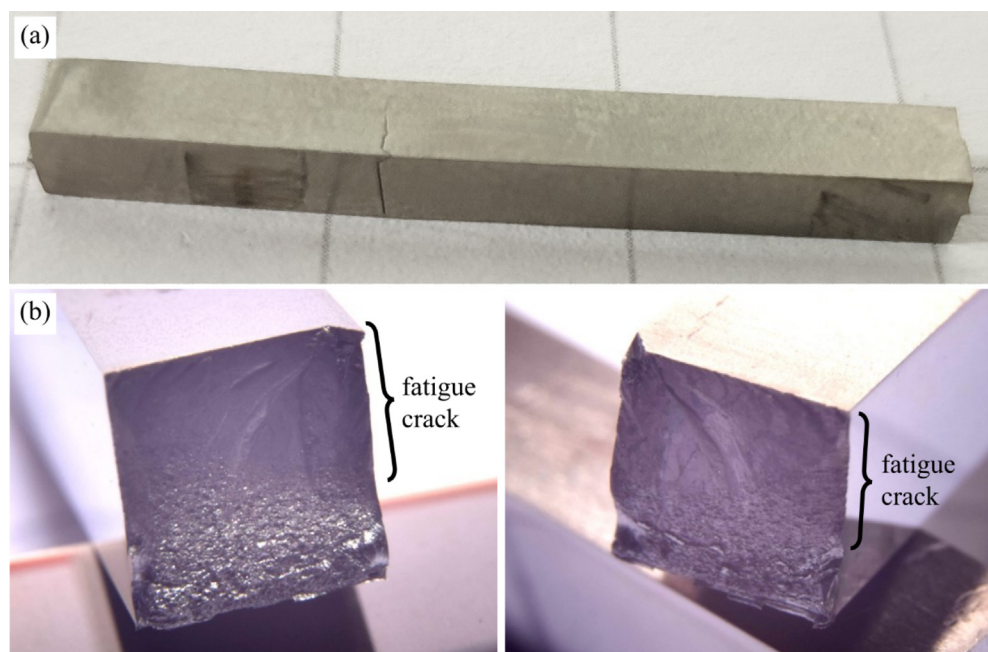


Fig. 9. (a) Zr₆₀Ti₂Nb₂Al_{7.5}Ni₁₀Cu_{18.5} fatigue test specimen (Row 15, Table 5) with fatigue crack partially extending through cross-section thickness. (b) Exposed fatigue crack fracture surfaces (smooth) after test specimen was mechanically separated (rough) after fatigue testing.

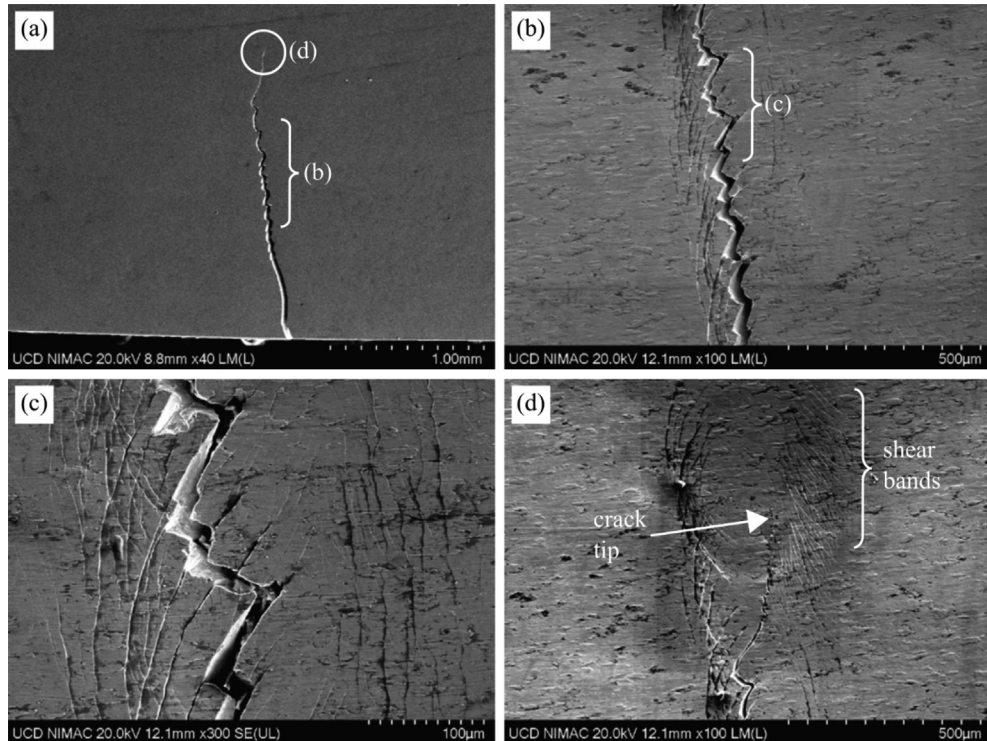


Fig. 10. SEM images of crack formed in $Zr_{60}Ti_2Nb_2Al_{7.5}Ni_{10}Cu_{18.5}$ test specimen during fatigue testing (Row 15, Table 5). (a) Full crack profile with bottom edge of test specimen apparent. (b) magnified portion of the fatigue crack exhibiting staircase-type crack morphology. (c) Magnified view of several of the steps apparent in the fatigue crack as well as local shear banding of the adjacent material. Step edges oriented $\sim 45^\circ$ from the direction of the applied cyclic load. (d) Shear bands developing ahead of the crack tip in the propagation direction.

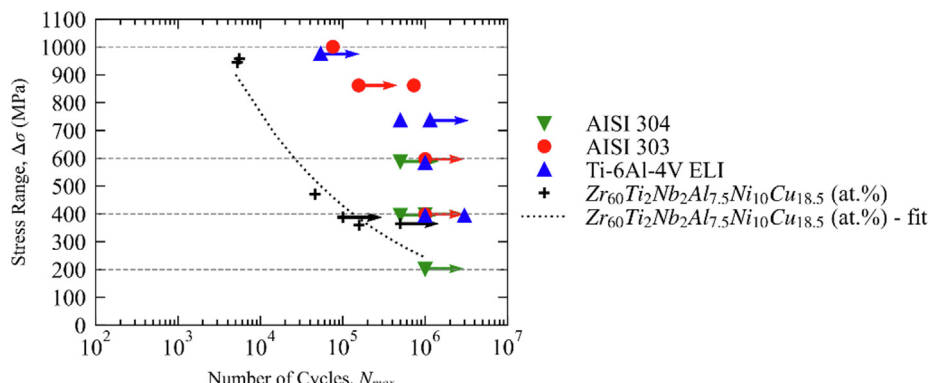


Fig. 11. S-N plots of fatigue rest results for AISI 304 stainless steel (cold worked), AISI 303 stainless steel (cold worked), and Ti-6Al-4 V ELI, along with $Zr_{60}Ti_2Nb_2Al_{7.5}Ni_{10}Cu_{18.5}$ (at.%) fatigue testing results shown previously in Fig. 7. Arrows indicate test specimens reached cycle target without failure. Dashed horizontal lines indicate nominal target stress ranges. Fit of $Zr_{60}Ti_2Nb_2Al_{7.5}Ni_{10}Cu_{18.5}$ (at.%) data points illustrates maximum performance threshold of selected BMG alloys.

mens exhibiting exceptional performance and those exhibiting relatively poor performance. For example, in relation to apparent plasticity, in Fig. 2 (a) showing the stress-strain response of compression test specimens produced from $Zr_{53}Al_{16}Co_{23.25}Ag_{7.75}$, curves (i) and (ii) are from the same batch, and (iii) to (vi) from a different batch. Evaluation of curves (i) and (ii) show that this composition exhibited some of the highest levels of plasticity, along with the highest strength, of the four alloys tested. However, the responses shown in curves (iii) to (vi) were more characteristic of this alloy's performance. The characteristics of each alloy are summarized below.

4.3. Alloy Performance: $Zr_{53}Al_{16}Co_{23.25}Ag_{7.75}$

As stated, $Zr_{53}Al_{16}Co_{23.25}Ag_{7.75}$ was found to exhibit extreme brittleness and no plasticity more commonly, as illustrated. Furthermore, regardless of the plasticity observed during compression testing of $Zr_{53}Al_{16}Co_{23.25}Ag_{7.75}$, specimens always shattered into a large number of tiny fragments, as shown in Fig. 3 (a). Arc melter-based processing of this alloy was also problematic with frequent and violent fracturing of sample buttons inside the chamber during initial melting. Sample buttons positioned on the water-cooled copper hearth would explode inside the chamber on ignition of the electric arc. High levels of porosity were also typical of suction cast geometries produced from this alloy. DSC characterization of $Zr_{53}Al_{16}Co_{23.25}Ag_{7.75}$ indicated the lowest potential for

thermoplastic formability, with a relatively small ΔT_x and short duration before the onset of crystallization above T_g , Fig. 6 (a). Extremely poor fatigue performance was observed, Fig. 7 (a), with only high cycle fatigue possible at the lowest stress range, $\Delta\sigma$.

4.4. Alloy Performance: $Zr_{49}Ti_{1.96}Cu_{37.24}Al_{9.8}Y_2$

Compression tests performed on $Zr_{49}Ti_{1.96}Cu_{37.24}Al_{9.8}Y_2$ revealed a similar performance, Fig. 2 (b), again with the curve (i) and (ii) coming from a different batch to curves (iii) to (vi). Additionally, curves (iii)-(iv) and (v)-(vi) were produced by test specimens from the same batch but from different BMG rods. Two test specimens from the same batch, (i) and (ii), both exhibited marked plasticity before fracture. The remaining four curves, from the same batch but cast at different times, exhibit similar stress-strain characteristics with limited plastic deformation. However, processability of the $Zr_{49}Ti_{1.96}Cu_{37.24}Al_{9.8}Y_2$ alloy was significantly improved over $Zr_{53}Al_{16}Co_{23.25}Ag_{7.75}$ during alloying and suction casting. This alloy exhibited a higher potential for thermoplastic forming, Fig. 6 (b), and its fatigue performance was improved, Fig. 7 (b).

4.5. Alloy Performance: $Zr_{60}Ti_2Nb_2Al_{7.5}Ni_{10}Cu_{18.5}$

Composition $Zr_{60}Ti_2Nb_2Al_{7.5}Ni_{10}Cu_{18.5}$ exhibited the best combination of processability, mechanical properties, potential for thermoplastic formability, and fatigue endurance of all the alloys tested. This is most evident in Fig. 2 (c), the stress-strain response exhibits no sample batch influence. In all cases a relatively high degree of plasticity was apparent prior to test specimen failure. Compression test specimens typically fragmented into two pieces along the plane of maximum shear stress. Fatigue testing of this composition revealed the L-shape S-N curve typical of crystalline metals, Fig. 7 (c). Fatigue endurance approaching the high cycle threshold (10^4 cycles) was achieved for the highest stress range investigated (1000 MPa). Furthermore, crack propagation was significantly restrained for this composition, exhibiting the staircase-type crack morphology described previously (Fig. 10). The process zone ahead of the crack tip resulted in shear band generation which caused the crack to change direction continuously fracturing continues. In Fig. 10 (c), orthogonally intersecting shear bands are evident to the left of the crack, which likely facilitated the resultant crack morphology. Using the extent of the shear banding apparent in Fig. 10 (d), $Zr_{60}Ti_2Nb_2Al_{7.5}Ni_{10}Cu_{18.5}$ appears to have a relatively large processing zone diameter ($\sim 400 \mu\text{m}$), which suggests particular applicability of this composition for thin flexures.

4.6. Alloy Performance: $Cu_{47}Zr_{46}Al_5Y_2$

Finally, alloy $Cu_{47}Zr_{46}Al_5Y_2$ also exhibited batch-independent mechanical properties and relatively high plasticity during compression testing, Fig. 2 (d). This alloy performed comparably to $Zr_{49}Ti_{1.96}Cu_{37.24}Al_{9.8}Y_2$, described previously. DSC scans of the two alloys are nominally similar (Fig. 5), as are the S-N plots of fatigue endurance. However, processability of this alloy was exceptionally poor relative to the other systems. High levels of porosity were typical regardless of as-cast geometry, and it proved a significant challenge to achieve fully amorphous castings consistently. This alloy has been the subject of several wear characterization [51,55,67] studies and has shown promising wear resistance in both standard testing and gear-on-gear testing. However, processing difficulties limit its suitability. It was also noted that, while the measured thermomechanical properties of the other three compositions tested were in line with their published results, the reported value of elastic modulus for $Cu_{47}Zr_{46}Al_5Y_2$ (~ 75 GPa) dif-

fered from the one calculated in this work (~ 87 GPa), as indicated in Table 2. The cause of this discrepancy is unclear.

All four compositions investigated had Zr and Al in common. Three of the four were of the common Zr-Cu-Al family of BMG alloys [16]. Cu, Co, and Ni are similarly sized atoms, exhibiting slightly different heats of mixing with other alloying elements, and are therefore expected to perform a similar function during rapid cooling in frustrating reordering and crystallization while the viscosity in the liquid increases. However, the substitution of cobalt for copper in $Zr_{53}Al_{16}Co_{23.25}Ag_{7.75}$ resulted in severe embrittlement of the alloy, significantly reducing its mechanical strength. However, $Zr_{53}Al_{16}Co_{23.25}Ag_{7.75}$ also exhibited the highest glass transition temperature, though the lowest glass forming ability. As the number of alloying elements increased, the glass forming ability improved, as illustrated in Table 4. The higher addition of copper in $Cu_{47}Zr_{46}Al_5Y_2$ resulted in the best wear performance of the four compositions tested [51]. However, the comparable $Zr_{49}Ti_{1.96}Cu_{37.24}Al_{9.8}Y_2$ alloy with added titanium exhibited comparable thermomechanical properties with higher glass forming ability and better processability.

4.7. BMG comparison with commercial alloys

Each of the commercial alloys tested exhibited good fatigue endurance for the stress ranges applied. The majority of the specimens tested reached the preselected cycle threshold ($\geq 10^6$ cycles) without fracture (indicated by arrows in Fig. 11). Premature failure in the high cycle fatigue range, was observed as the stress range increased to the maximum level, 1000 MPa. Comparing the data in Fig. 11 with the BMG fatigue testing results in Fig. 7, the BMG alloys performed significantly poorer in fatigue than the commercial alloys, particularly at higher stress ranges. At a stress range of 400 MPa composition $Zr_{60}Ti_2Nb_2Al_{7.5}Ni_{10}Cu_{18.5}$ exhibited comparable fatigue endurance to the commercial alloys. While a significantly more fatigue testing is required to fully characterize the BMG fatigue performance, based on these preliminary results, the alloy $Zr_{60}Ti_2Nb_2Al_{7.5}Ni_{10}Cu_{18.5}$ exhibits potential for fatigue applications, e.g., flexure-based compliant mechanisms. In conjunction with the work presented herein, the four alloys of interest were previously investigated for wear performance [51], which is of particular interest in gearing applications, using a ball-on-disc (BOD) wear testing apparatus. The wear resistance of the four the BMG alloys were also compared to standard commercial alloys under the same testing conditions. The specific wear rate, K , of each alloy tested is shown in Fig. 12. Three of the BMG alloys ($Zr_{53}Al_{16}Co_{23.25}Ag_{7.75}$, $Zr_{49}Ti_{1.96}Cu_{37.24}Al_{9.8}Y_2$, and $Cu_{47}Zr_{46}Al_5Y_2$) exhibited favorable wear resistance, better than or comparable to the commercial alloys. The $Zr_{60}Ti_2Nb_2Al_{7.5}Ni_{10}Cu_{18.5}$ alloy exhibited a similar wear performance as Ti-6Al-4 V, a commonly used light metal alloy in aerospace applications.

5. Conclusions & future work

A substantial number of BMG compositions have been presented in the literature to date, with more being developed and characterized annually. While much of the research into BMGs has been on alloy development, few have focused on a systematic analysis of specific compositions performance for particular applications.

It should be noted that the selection criteria used in this work was somewhat restrictive, eliminating compositions requiring exotic or prohibitively expensive elements. For example, beryllium containing compositions, which are typically excellent glass formers [20], and platinum/palladium compositions, which have exhibited some of the largest critical casting diameters achieved [21].

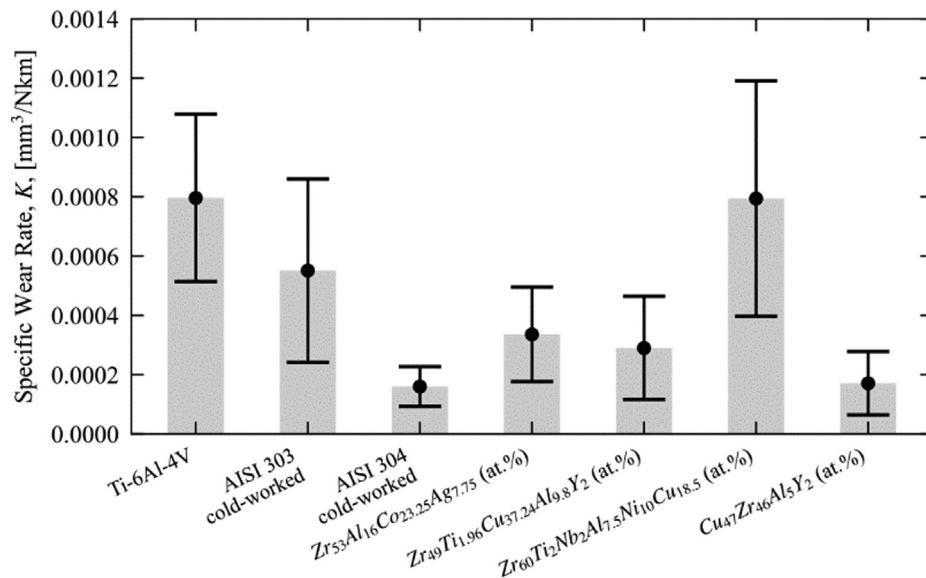


Fig. 12. Calculated average specific wear rate, K , grouped by composition. Error bars represent one standard deviation from the calculated mean.

This approach was selected to characterize more general-purpose BMG compositions for typical space mechanisms requirements. However, for particularly advanced space applications, where processing complexities and/or cost implications may be secondary concerns, there may be no need of such limits. For the selection criteria chosen, the majority of appropriate BMGs were of the Zr-Cu-Al family, with variations of element additions and composition. The alloys were characterized for strength (via compression testing), thermoplastic formability and operating temperature range, and fatigue endurance. Fatigue performance was not as good as that of conventional crystalline alloys, but may be sufficient if stress levels are kept relatively low by design. Characterization of the hardness and wear performance of these alloys has already been presented [51]. Additionally, the processability of each alloy was of particular interest. Two of the four compositions (Zr-Al-Co-Ag and Cu-Zr-Al-Y) exhibited frequently high levels of porosity and pour mold filling resulted in poor cooling conditions which prevented achieving fully amorphous castings. Conversely, these alloys exhibited the highest strengths, hardness, and plasticity (Zr-Al-Co-Ag), as well as the enhanced wear resistance in laboratory testing (Cu-Zr-Al-Y) [51]. The remaining two alloys: Zr-Ti-Cu-Al-Y and Zr-Ti-Nb-Al-Ni-Cu, exhibited significantly improved processability. The Zr-Ti-Nb-Al-Ni-Cu system exhibited the best overall processability, high levels of plasticity, and relatively good fatigue endurance. Its fracture characteristics suggest potential benefits in applications where debris mitigation is a requirement in the event of failure, e.g., space-based operations. In all cases test specimens manufactured from Zr-Ti-Nb-Al-Ni-Cu fractured into two large pieces, as opposed to many fragments as was observed with the other alloys.

The results of this work, and the study published previously [51], suggest the two best candidate alloys for further investigation are Zr₄₉Ti_{1.96}Cu_{37.24}Al_{9.8}Y₂ (at.%) [53] and Zr₆₀Ti₂Nb₂Al_{7.5}Ni₁₀Cu_{18.5} (at.%) [54], for gearing applications and flexure-based mechanisms, respectively. Gearing applications require high strength, wear resistance, toughness, and fatigue endurance. When incorporating good processability into the selection criteria, Zr₄₉Ti_{1.96}Cu_{37.24}Al_{9.8}-Y₂ (at.%) exhibited the best combination of properties most suitable for gearing applications. For flexures, high elastic limit, toughness, and fatigue endurance of most importance. While the elastic limits of all BMG alloys are comparable, the fatigue performance of Zr₆₀Ti₂Nb₂Al_{7.5}Ni₁₀Cu_{18.5} (at.%) was found to be the best

of the four BMG alloys tested. Practical testing of components manufactured from these alloys is currently underway. It is planned to carry out testing of the selected BMG alloys under non-ambient conditions like those experienced in space; including at elevated and cryogenic temperatures and under vacuum conditions; successful completion is expected to lead to future space-based applications. A summary of the values obtained for the thermomechanical characterization of the four BMG compositions investigated as part of this work is given in Table 6. Further refinement of processing and casting parameters are also warranted to better improve the success rate of BMG component manufacturing.

Data availability

The data that support the findings of this study are available from the corresponding author upon reasonable request.

Declaration of Competing Interest

The authors declare that they have no known competing financial interests or personal relationships that could have appeared to influence the work reported in this paper.

Acknowledgements

Funding for this work was provided by the European Space Agency (ESA) under the project: *Metallic Glasses for High Performance Mechanism Applications on Long Term Missions*, CN: 4000127199/19/NL/AR/zk.

The authors would like to thank Dr Ian Reid of the UCD Nano Imaging and Material Analysis Centre (NIMAC) for his assistance with SEM/EDX characterization.

The authors would also like to thank Mr. Rik Stewart (formerly of Reliance Precision, UK), Mr. Martin Humphries (SpaceMech, UK), and Dr Tom Worsley (Reliance Precision, UK) for their fruitful discussions of practical space mechanism requirements, and Mr. Tadg Collins or Reliance Precision Manufacturing Ireland for the provision of titanium alloy and steel samples for comparison testing.

Table 6

Experimentally determined thermophysical properties of each of the four compositions investigated and comparable commercial metals, where E is the Young's modulus, ε_e is the elastic strain limit, ε_p is the plastic strain limit, σ_y is the yield stress, HV is the Vickers hardness, T_g is the glass transition temperature, T_x is the crystallisation temperature, ΔT_x is the SCLR, K is the specific wear rate, and σ_e is the fatigue endurance stress limit.*estimated values based on experimental results.

| Composition (at.%) | E [GPa] | ε_e [%] | ε_p [%] | σ_y [GPa] | HV [kgf-mm $^{-2}$] | T_g [°C] | T_x [°C] | ΔT_x [°C] | K [mm 3 .N $^{-1}$.km $^{-1}$] | $*\sigma_e$ [MPa] |
|--|-----------|---------------------|---------------------|------------------|----------------------|------------|------------|-------------------|---------------------------------------|-------------------|
| Zr ₅₃ Al ₁₆ Co _{23.25} Ag _{7.75} | 94 ± 3 | 2.0 ± 0.1 | 0.7 ± 0.9 | 1.9 ± 0.0 | 577 ± 36 | 483 | 516 | 33 | 0.34 × 10 $^{-3}$ ± 0.16 × 10 $^{-3}$ | < 200 |
| Zr ₄₉ Ti _{1.96} Cu _{37.24} Al _{9.8} Y ₂ | 87 ± 3 | 1.9 ± 0.1 | 0.5 ± 0.5 | 1.6 ± 0.1 | 527 ± 51 | 400 | 470 | 70 | 0.29 × 10 $^{-3}$ ± 0.17 × 10 $^{-3}$ | < 400 |
| Zr ₆₀ Ti ₂ Nb ₂ Al _{7.5} Ni ₁₀ Cu _{18.5} | 80 ± 3 | 1.8 ± 0.1 | 1.1 ± 0.6 | 1.5 ± 0.1 | 426 ± 11 | 378 | 446 | 68 | 0.79 × 10 $^{-3}$ ± 0.40 × 10 $^{-3}$ | < 400 |
| Cu ₄₇ Zr ₄₆ Al ₅ Y ₂ | 87 ± 2 | 1.9 ± 0.1 | 0.8 ± 0.2 | 1.6 ± 0.1 | 478 ± 32 | 407 | 468 | 61 | 0.17 × 10 $^{-3}$ ± 0.11 × 10 $^{-3}$ | < 400 |
| AISI 303 (cold worked) | 196 ± 4 | 0.3 ± 0.1 | 30 ± 10 | 0.6 ± 0.1 | 277 ± 26 | N/A | N/A | N/A | 0.55 × 10 $^{-3}$ ± 0.31 × 10 $^{-3}$ | < 600 |
| AISI 304 (cold worked) | 197 ± 6 | 0.3 ± 0.0 | 20 ± 10 | 0.6 ± 0.1 | 268 ± 17 | N/A | N/A | N/A | 0.16 × 10 $^{-3}$ ± 0.07 × 10 $^{-3}$ | < 800 |
| Ti-6Al-4 V ELL, Annealed | 114 ± 3 | 0.7 ± 0.1 | 15 ± 5 | 0.8 ± 0.1 | 308 ± 14 | N/A | N/A | N/A | 0.80 × 10 $^{-3}$ ± 0.28 × 10 $^{-3}$ | < 800 |

Data Availability Statement.

The data that support the findings of this study are available from the corresponding author upon reasonable request.

Appendix A

The isothermal scans performed for each of the four BMG composition is shown in [Figure A1](#). The legend in each sub-figure indicates the isothermal hold temperature and the test specimen mass. The magnitude of the heat flow is irrelevant for this work, and all scan curves are artificially vertically offset to maintain a suitable spacing. The initial constant heating heat flow vs time data was omitted from [Figure A1](#), with the \blacktriangle marker indicating the time when T_g was reached, and the \blacktriangledown marker indicating the time when the isothermal hold temperature, T_{iso} , was reached. Each test commenced ($t = 0$ min) with the specimen at room temperature. Once the pre-set T_{iso} temperature was reached, the system software sta-

bilized the temperature in the chamber and held until crystallization had concluded. The thermal controller was slightly underdamped resulting in an overshoot of ~ 1.5 °C and a settling time of ~ 1.5 s. On each scan curve the time of peak crystallization is indicated by a + marker.

Appendix B

A list of the 4 PB fatigue tests performed in this work is given in [Table B1](#). The measured test specimen widths (B) and heights (H) are listed in columns 10 and 11, respectively. These measurements were used to calculate the stress ranges experience by the test specimen during fatigue testing using Eqn. (1). The \rightarrow symbol in rows 5, 6, 12, 16, 18, 19, and 25 indicate that these test specimens reached N_{max} without failure. The \dagger symbol in rows 9, 14, 16, and 17 highlights test specimens where fatigue testing was paused, and the test specimen examined for any crack development. The test specimen was then replaced back into the fatigue tester

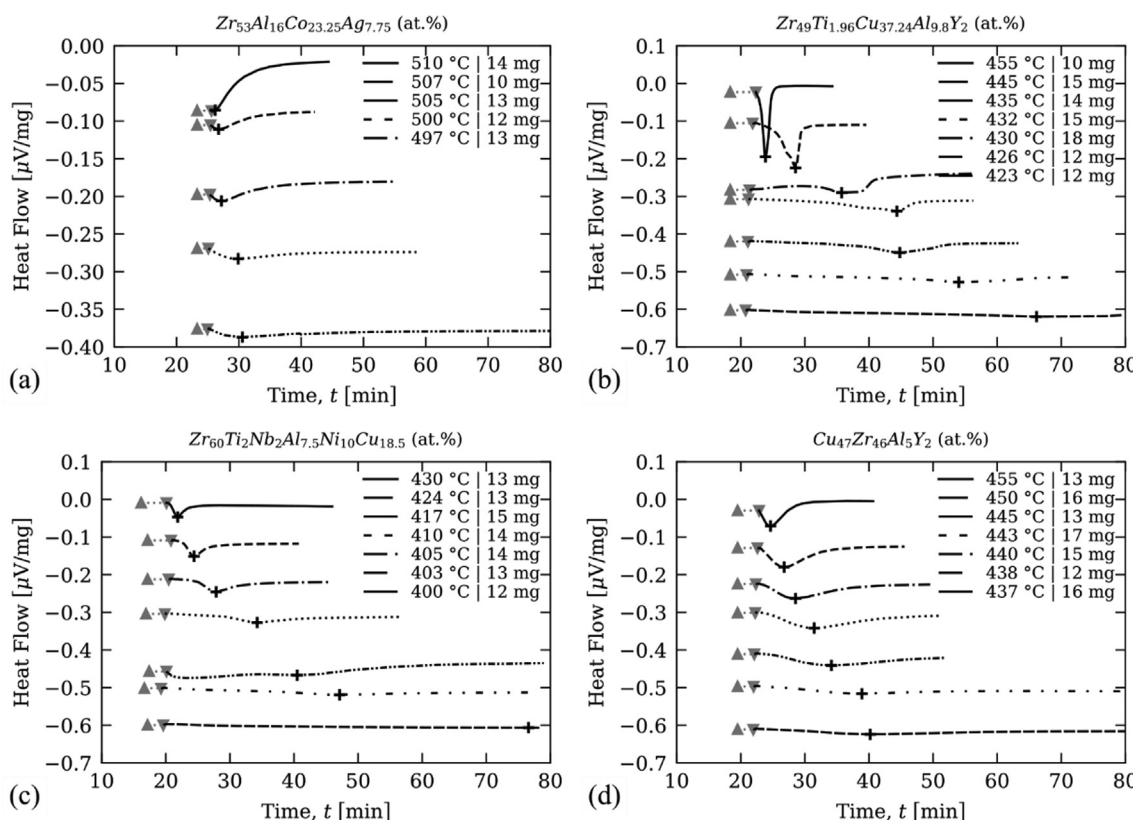


Fig. A1. Isothermal DSC scans performed on the Netzsch Polyma 214 DSC with pre-isothermal hold heat flow data removed. (a) Zr₅₃Al₁₆Co_{23.25}Ag_{7.75} (at.%), (b) Zr₄₉Ti_{1.96}Cu_{37.24}Al_{9.8}Y₂ (at.%), (c) Zr₆₀Ti₂Nb₂Al_{7.5}Ni₁₀Cu_{18.5} (at.%), and (d) Cu₄₇Zr₄₆Al₅Y₂ (at.%). Isothermal hold temperatures indicated in legend. In each sub-figure, the time when T_g was reached (\blacktriangle), the time when T_{iso} was reached (\blacktriangledown), and the time when peak crystallization occurred (+) are also indicated.

Table B1

List of 4 PB fatigue testing experiments performed along with variable test parameters. Constant parameters for all tests: $f_z = 25$ Hz, $L \cong 30$ mm, $S_1 = 10$ mm, and $S_2 = 20$ mm.

| # | Composition (at.%) | F_{mid} | F | F_a | F_{min} | F_{max} | N_{fade} | d_r | B | H |
|----|--|------------------|-----|-------|------------------|------------------|-------------------|-------|------|------|
| 1 | Zr ₅₃ Al ₁₆ Co _{23.25} Ag _{7.75} | 1100 | 10 | 900 | 200 | 2000 | 125 | 6 | 3.09 | 3.10 |
| 2 | Zr ₅₃ Al ₁₆ Co _{23.25} Ag _{7.75} | 660 | 5 | 540 | 120 | 1200 | 25 | 6 | 3.13 | 3.10 |
| 3 | Zr ₅₃ Al ₁₆ Co _{23.25} Ag _{7.75} | 440 | 5 | 360 | 80 | 800 | 25 | 5 | 3.08 | 3.09 |
| 4 | Zr ₅₃ Al ₁₆ Co _{23.25} Ag _{7.75} | 440 | 5 | 360 | 80 | 800 | 25 | 5 | 3.10 | 3.09 |
| 5 | Zr ₅₃ Al ₁₆ Co _{23.25} Ag _{7.75} | 220 | 5 | 180 | 40 | 400 | 25 | 5 | 3.05 | 3.04 |
| 6 | Zr ₅₃ Al ₁₆ Co _{23.25} Ag _{7.75} | 220 | 5 | 180 | 40 | 400 | 25 | 5 | 3.04 | 3.05 |
| 7 | Zr ₄₉ Ti _{1.96} Cu _{37.24} Al _{9.8} Y ₂ | 1100 | 10 | 900 | 200 | 2000 | 125 | 6 | 3.17 | 3.15 |
| 8 | Zr ₄₉ Ti _{1.96} Cu _{37.24} Al _{9.8} Y ₂ | 660 | 5 | 540 | 120 | 1200 | 25 | 6 | 3.10 | 3.10 |
| 9 | Zr ₄₉ Ti _{1.96} Cu _{37.24} Al _{9.8} Y ₂ | 440 | 5 | 360 | 80 | 800 | 25 | 5 | 3.09 | 3.11 |
| 10 | Zr ₄₉ Ti _{1.96} Cu _{37.24} Al _{9.8} Y ₂ | 440 | 5 | 360 | 80 | 800 | 25 | 5 | 3.10 | 3.10 |
| 11 | Zr ₄₉ Ti _{1.96} Cu _{37.24} Al _{9.8} Y ₂ | 440 | 5 | 360 | 80 | 800 | 25 | 5 | 3.01 | 3.02 |
| 12 | Zr ₄₉ Ti _{1.96} Cu _{37.24} Al _{9.8} Y ₂ | 440 | 5 | 360 | 80 | 800 | 25 | 5 | 3.05 | 3.03 |
| 13 | Zr ₆₀ Ti ₂ Nb ₂ Al _{7.5} Ni ₁₀ Cu _{18.5} | 1100 | 1 | 900 | 200 | 2000 | 10 | 6 | 3.05 | 3.06 |
| 14 | Zr ₆₀ Ti ₂ Nb ₂ Al _{7.5} Ni ₁₀ Cu _{18.5} | 1100 | 10 | 900 | 200 | 2000 | 125 | 6 | 3.07 | 3.03 |
| 15 | Zr ₆₀ Ti ₂ Nb ₂ Al _{7.5} Ni ₁₀ Cu _{18.5} | 660 | 5 | 540 | 120 | 1200 | 25 | 6 | 3.26 | 3.25 |
| 16 | Zr ₆₀ Ti ₂ Nb ₂ Al _{7.5} Ni ₁₀ Cu _{18.5} | 440 | 5 | 360 | 80 | 800 | 25 | 5 | 3.10 | 3.09 |
| 17 | Zr ₆₀ Ti ₂ Nb ₂ Al _{7.5} Ni ₁₀ Cu _{18.5} | 440 | 5 | 360 | 80 | 800 | 25 | 5 | 3.10 | 3.11 |
| 18 | Zr ₆₀ Ti ₂ Nb ₂ Al _{7.5} Ni ₁₀ Cu _{18.5} | 440 | 5 | 360 | 80 | 800 | 25 | 5 | 3.02 | 3.03 |
| 19 | Zr ₆₀ Ti ₂ Nb ₂ Al _{7.5} Ni ₁₀ Cu _{18.5} | 440 | 5 | 360 | 80 | 800 | 25 | 5 | 3.04 | 3.03 |
| 20 | Cu ₄₇ Zr ₄₆ Al ₅ Y ₂ | 1100 | 10 | 900 | 200 | 2000 | 125 | 6 | 3.17 | 3.25 |
| 21 | Cu ₄₇ Zr ₄₆ Al ₅ Y ₂ | 660 | 5 | 540 | 120 | 1200 | 25 | 6 | 3.16 | 3.19 |
| 22 | Cu ₄₇ Zr ₄₆ Al ₅ Y ₂ | 440 | 5 | 360 | 80 | 800 | 25 | 5 | 3.11 | 3.08 |
| 23 | Cu ₄₇ Zr ₄₆ Al ₅ Y ₂ | 440 | 5 | 360 | 80 | 800 | 25 | 5 | 3.10 | 3.09 |
| 24 | Cu ₄₇ Zr ₄₆ Al ₅ Y ₂ | 440 | 5 | 360 | 80 | 800 | 25 | 5 | 3.02 | 3.01 |
| 25 | Cu ₄₇ Zr ₄₆ Al ₅ Y ₂ | 440 | 5 | 360 | 80 | 800 | 25 | 5 | 3.03 | 3.04 |

and the testing restarted. Columns 3 and 4 show the encoder-recorded maximum and minimum displacement of the crosshead during fatigue testing, respectively. The values for stress in columns 6 to 10 were calculated based on the test specimen geometry in conjunction with Eqn. (1). Absent data in row 1 indicates that test specimen failure before reaching the mid load, F_{mid} , so no fatigue test data was recorded. The zero value for maximum number of cycles in row 7 indicates tests specimen failure prematurely during the fade-in period, N_{fade} .

References

- J.P. Grotzinger, J. Crisp, A.R. Vasavada, R.C. Anderson, C.J. Baker, R. Barry, D.F. Blake, P. Conrad, K.S. Edgett, B. Ferdowski, R. Gellert, J.B. Gilbert, M. Golombek, J. Gómez-Elvira, D.M. Hassler, L. Jandura, M. Litvak, P. Mahaffy, J. Maki, M. Meyer, M.C. Malin, I. Mitrofanov, J.J. Simmonds, D. Vaniman, R.V. Welch, R.C. Wiens, Mars Science Laboratory Mission and Science Investigation, Space Sci. Rev. 170 (2012) 5–56, <https://doi.org/10.1007/s11214-012-9892-2>.
- P. Fortescue, G. Swinerd, J. Stark (Eds.), *Spacecraft Systems Engineering*, 4th ed., Wiley, 2011.
- M.F. Ashby, *Materials Selection in Mechanical design*, 2nd ed., Butterworth-Heinemann, 1999.
- S. Lewis, M. Humphries, An Introduction to Bearing Active Preload Systems-technology and Performance Benefits, in: Proc. 11supthsup Eur. Space Mech. Tribol. Symp. – ESMATS 21 – 23 Sept., Lucerne, Switzerland, 2005: pp. 261–269.
- R.M. Fowler, L.L. Howell, S.P. Magleby, Compliant Space Mechanisms: A New Frontier for Compliant Mechanisms, Mech. Sci. 2 (2011) 205–215, <https://doi.org/10.5194/ms-2-205-2011>.
- W. Klement, R.H. Willens, P. Duwez, Non-crystalline Structure in Solidified Gold-Silicon Alloys, Nature. 187 (1960) 869, <https://doi.org/10.1038/187869b0>.
- H.S. Chen, Thermodynamic considerations on the formation and stability of metallic glasses, Acta Metall. 22 (1974) 1505–1511, [https://doi.org/10.1016/0001-6160\(74\)90112-6](https://doi.org/10.1016/0001-6160(74)90112-6).
- M.F. Ashby, A.L. Greer, Metallic Glasses as Structural Materials, Scr. Mater. 54 (2006) 321–326, <https://doi.org/10.1016/j.scriptamat.2005.09.051>.
- J.J. Krizic, Bulk Metallic Glasses as Structural Materials: A Review, Adv. Eng. Mater. 18 (2016) 1308–1331, <https://doi.org/10.1002/adem.201600066>.
- A.L. Greer, Metallic Glasses... On The Threshold, Mater. Today. 12 (2009) 14–22, [https://doi.org/10.1016/S1369-7021\(09\)70037-9](https://doi.org/10.1016/S1369-7021(09)70037-9).
- M. Jafary-Zadeh, G. Praveen Kumar, P.S. Branicio, M. Seifi, J.J. Lewandowski, F. Cui, A Critical Review on Metallic Glasses as Structural Materials for Cardiovascular Stent Applications, J. Funct. Biomater. 9 (2018), <https://doi.org/10.3390/jfb9010019>.
- C. Suryanarayana, A. Inoue, *Bulk Metallic Glasses*, 2nd ed., CRC Press, 2017, <https://doi.org/10.1201/9781315153483>.
- M.K. Miller, P. Liaw (Eds.), *Bulk Metallic Glasses: An Overview*, Springer, US, 2008. <https://www.springer.com/gp/book/9780387489209> (accessed August 30, 2019).
- J.F. Löfller, Bulk Metallic Glasses, Intermetallics. 11 (2003) 529–540, [https://doi.org/10.1016/S0966-9795\(03\)00046-3](https://doi.org/10.1016/S0966-9795(03)00046-3).
- J. Schroers, Processing of Bulk Metallic Glass, Adv. Mater. 22 (2010) 1566–1597, <https://doi.org/10.1002/adma.200902776>.
- Y. Li, S. Zhao, Y. Liu, P. Gong, J. Schroers, How Many Bulk Metallic Glasses Are There?, ACS Comb. Sci. 19 (2017) 687–693, <https://doi.org/10.1021/acscombsci.7b00048>.
- C.-Y. Chen, Insight into Bulk Metallic Glass Technology Development Trajectory: Mapping from Patent Information Analysis, Solid State Phys. (2018), <https://doi.org/10.5772/intechopen.81733>.
- R. Hasegawa, M.C. Narasimhan, N. DeCristofaro, A high permeability Fe-Ni base glassy alloy containing Mo, J. Appl. Phys. 49 (1978) 1712–1714, <https://doi.org/10.1063/1.324897>.
- A. Inoue, T. Zhang, T. Masumoto, Zr-Al-Ni Amorphous Alloys with High Glass Transition Temperature and Significant Supercooled Liquid Region, Mater. Trans. JIM. 31 (1990) 177–183, <https://doi.org/10.2320/matertrans1989.31.177>.
- A. Peker, W.L. Johnson, A Highly Processable Metallic Glass: Zr_{41.2}Ti_{13.8}Cu_{12.5}Ni_{10.0}Be_{2.25}, Appl. Phys. Lett. 63 (1993) 2342–2344, <https://doi.org/10.1063/1.110520>.
- N. Nishiyama, K. Takenaka, H. Miura, N. Saidoh, Y. Zeng, A. Inoue, The World's Biggest Glassy Alloy Ever Made, Intermetallics. 30 (2012) 19–24, <https://doi.org/10.1016/j.intermet.2012.03.020>.
- A. Inoue, B. Shen, H. Koshiba, H. Kato, A.R. Yavari, Cobalt-based Bulk Glassy Alloy with Ultrahigh Strength and Soft Magnetic Properties, Nat. Mater. 2 (2003) 661, <https://doi.org/10.1038/nmat982>.
- D.C. Hofmann, J.-Y. Suh, A. Wiest, G. Duan, M.-L. Lind, M.D. Demetriou, W.L. Johnson, Designing Metallic Glass Matrix Composites with High Toughness and Tensile Ductility, Nature. 451 (2008) 1085–1089, <https://doi.org/10.1038/nature06598>.
- C.A. Schuh, T.C. Hufnagel, U. Ramamurthy, Mechanical Behavior of Amorphous Alloys, Acta Mater. 55 (2007) 4067–4109, <https://doi.org/10.1016/j.actamat.2007.01.052>.
- A.L. Greer, Y.Q. Cheng, E. Ma, Shear Bands in Metallic Glasses, Mater. Sci. Eng. R Rep. 74 (2013) 71–132, <https://doi.org/10.1016/j.mser.2013.04.001>.
- R.D. Conner, W.L. Johnson, N.E. Paton, W.D. Nix, Shear Bands and Cracking of Metallic Glass Plates in Bending, J. Appl. Phys. 94 (2003) 904–911, <https://doi.org/10.1063/1.1582555>.
- R.D. Conner, Y. Li, W.D. Nix, W.L. Johnson, Shear Band Spacing under Bending of Zr-based Metallic Glass Plates, Acta Mater. 52 (2004) 2429–2434, <https://doi.org/10.1016/j.actamat.2004.01.034>.
- D.C. Hofmann, J.-Y. Suh, A. Wiest, M.-L. Lind, M.D. Demetriou, W.L. Johnson, Development of Tough, Low-Density Titanium-Based Bulk Metallic Glass Matrix Composites with Tensile Ductility, Proc. Natl. Acad. Sci. 105 (2008) 20136–20140, <https://doi.org/10.1073/pnas.0809000106>.
- D.C. Hofmann, J.-Y. Suh, A. Wiest, W. Johnson, New Processing Possibilities for Highly Toughened Metallic Glass Matrix Composites with Tensile Ductility,

- Scr. Mater. 59 (2008) 684–687, <https://doi.org/10.1016/j.scriptamat.2008.05.046>.
- [30] J.J. Krusic, Understanding the Problem of Fatigue in Bulk Metallic Glasses, Metall. Mater. Trans. A. 42 (2011) 1516–1523, <https://doi.org/10.1007/s11661-010-0413-1>.
- [31] C. Gilbert, J. Lippmann, R. Ritchie, Fatigue of a Zr-Ti-Cu-Ni-Be Bulk Amorphous Metal: Stress/Life and Crack-growth Behavior, Scr. Mater. 38 (1998) 537–542.
- [32] M.E. Launey, R. Busch, J.J. Krusic, Influence of Structural Relaxation on the Fatigue Behavior of a $Zr_{41.25}Ti_{13.75}Ni_{10}Cu_{12.5}Be_{22.5}$ Bulk Amorphous Alloy, Scr. Mater. 54 (2006) 483–487, <https://doi.org/10.1016/j.scriptamat.2005.09.048>.
- [33] G.Y. Wang, P.K. Liaw, M.L. Morrison, Progress in Studying the Fatigue Behavior of Zr-based Bulk Metallic Glasses and their Composites, Intermetallics. 17 (2009) 579–590, <https://doi.org/10.1016/j.intermet.2009.01.017>.
- [34] W.H. Peter, P.K. Liaw, R.A. Buchanan, C.T. Liu, C.R. Brooks, J.A. Horton, C.A. Carmichael, J.L. Wright, Fatigue Behavior of $Zr_{52.5}Al_{10}Ti_5Cu_{17.9}Ni_{14.6}$ Bulk Metallic Glass, Intermetallics. 10 (2002) 1125–1129, [https://doi.org/10.1016/S0966-9795\(02\)00152-8](https://doi.org/10.1016/S0966-9795(02)00152-8).
- [35] G.Y. Wang, P.K. Liaw, W.H. Peter, B. Yang, Y. Yokoyama, M.L. Benson, B.A. Green, M.J. Kirkham, S.A. White, T.A. Saleh, R.L. McDaniels, R.V. Steward, R.A. Buchanan, C.T. Liu, C.R. Brooks, Fatigue Behavior of Bulk Metallic Glasses, Intermetallics. 12 (2004) 885–892, <https://doi.org/10.1016/j.intermet.2004.02.043>.
- [36] M.E. Launey, D.C. Hofmann, W.L. Johnson, R.O. Ritchie, Solution to the Problem of the Poor Cyclic Fatigue Resistance of Bulk Metallic Glasses, Proc. Natl. Acad. Sci. 106 (2009) 4986–4991, <https://doi.org/10.1073/pnas.0900740106>.
- [37] K. Boopathy, D.C. Hofmann, W.L. Johnson, U. Ramamurthy, Near-threshold Fatigue Crack Growth in Bulk Metallic Glass Composites, J. Mater. Res. 24 (2009) 3611–3619, <https://doi.org/10.1557/jmr.2009.0439>.
- [38] S.E. Naleway, R.B. Greene, B. Gludovatz, N.K.N. Dave, R.O. Ritchie, J.J. Krusic, A Highly Fatigue-Resistant Zr-Based Bulk Metallic Glass, Metall. Mater. Trans. A. 44 (2013) 5688–5693, <https://doi.org/10.1007/s11661-013-1923-4>.
- [39] S.J. Hales, D.E. Stegall, Qualifying Bulk Metallic Glass Gear Materials for Spacecraft Applications, NASA, NASA Langley Research Center; Hampton, VA, United States, 2018. <https://ntrs.nasa.gov/search.jsp?R=20190001052> (accessed October 17, 2019).
- [40] D.C. Hofmann, Castable Amorphous Metal Mirrors and Mirror Assemblies, NASA Tech Briefs. (2013) 13–14.
- [41] T. Štefanov, H.V.R. Maraka, P. Meagher, J. Rice, W. Sillekens, D.J. Browne, Thin Film Metallic Glass Broad-spectrum Mirror Coatings for Space Telescope Applications, J. Non-Cryst. Solids X. 7 (2020) 1–8, <https://doi.org/10.1016/j.nocx.2020.100050>.
- [42] M. Davidson, S. Roberts, G. Castro, R.P. Dillon, A. Kunz, H. Kozachkov, M.D. Demetriou, W.L. Johnson, S. Nutt, D.C. Hofmann, Investigating Amorphous Metal Composite Architectures as Spacecraft Shielding, Adv. Eng. Mater. 15 (2013) 27–33, <https://doi.org/10.1002/adem.201200313>.
- [43] L. Hamill, S. Roberts, M. Davidson, W.L. Johnson, S. Nutt, D.C. Hofmann, Hypervelocity Impact Phenomenon in Bulk Metallic Glasses and Composites, Adv. Eng. Mater. 16 (2014) 85–93, <https://doi.org/10.1002/adem.201300252>.
- [44] D.C. Hofmann, L. Hamill, E. Christiansen, S. Nutt, Hypervelocity Impact Testing of a Metallic Glass-Stuffed Whipple Shield, Adv. Eng. Mater. 17 (2015) 1313–1322, <https://doi.org/10.1002/adem.201400518>.
- [45] D.C. Hofmann, R. Polit-Casillas, S.N. Roberts, J.-P. Borgonia, R.P. Dillon, E. Hilgemann, J. Kolodziejska, L. Montemayor, J. Suh, A. Hoff, K. Carpenter, A. Parness, W.L. Johnson, A. Kennett, B. Wilcox, Castable Bulk Metallic Glass Strain Wave Gears: Towards Decreasing the Cost of High-Performance Robotics, Sci. Rep. 6 (2016) 1–11, <https://doi.org/10.1038/srep37773>.
- [46] D.C. Hofmann, P. Bordeenithikasem, Z. Dawson, L. Hamill, R.P. Dillon, B. McEnerney, S. Nutt, S.C. Bradford, Investigating Bulk Metallic Glasses as Ball-and-Cone Locators for Spacecraft Deployable Structures, Aerosp. Sci. Technol. 82–83 (2018) 513–519, <https://doi.org/10.1016/j.ast.2018.10.004>.
- [47] P. Bordeenithikasem, S.N. Roberts, D.C. Hofmann, J.M. Ratliff, B.R. Greene, J.B. Bacon, S. Sohn, J. Schroers, Measuring Demisability of Bulk Metallic Glasses for Potential Satellite Applications Through Ablation Experiments, Adv. Eng. Mater. 22 (2020) 1–6, <https://doi.org/10.1002/adem.202000708>.
- [48] A. Grimberg, H. Baur, P. Bochsler, F. Bühl, D.S. Burnett, C.C. Hays, V.S. Heber, A.J.G. Jurewicz, R. Wieler, Solar Wind Neon from Genesis: Implications for the Lunar Noble Gas Record, Science. 314 (2006) 1133–1135, <https://doi.org/10.1126/science.1133568>.
- [49] A.J.G. Jurewicz, D.S. Burnett, R. Wiens, T.A. Friedmann, C. Hays, R. Hohlfelder, K. Nishiizumi, J.A. Stone, B. H., A. Butterworth, A.J. Campbell, M. Ebihara, I. Franchi, V. Heber, C. Hohenberg, M. Humayun, K. McKeegan, K. McNamara, R. Wieler, The Genesis Solar-Wind Collector Materials, Space Sci. Rev. 105 (2003) 535–560. doi:<https://doi.org/10.1023/A:1024469927444>.
- [50] M. Mohr, D.C. Hofmann, H.-J. Fecht, Thermophysical Properties of an $Fe_{57.75}Ni_{19.25}Mo_{10}C_2B_8$ Glass-Forming Alloy Measured in Microgravity, Adv. Eng. Mater. 23 (2021) 2001143. doi:<https://doi.org/10.1002/adem.202001143>.
- [51] A.G. Murphy, A. Norman, P. Meagher, D.J. Browne, Wear of Bulk Metallic Glass Alloys for Space Mechanism Applications, J. Tribol. 144 (2022), <https://doi.org/10.1115/1.4054146>.
- [52] N. Hua, S. Pang, Y. Li, J. Wang, R. Li, K. Georgarakis, A.R. Yavari, G. Vaughan, T. Zhang, Ni- and Cu-free Zr-Al-Co-Ag Bulk Metallic Glasses with Superior Glass-forming Ability, J. Mater. Res. 26 (2011) 539–546, <https://doi.org/10.1557/jmr.2010.65>.
- [53] K. Zhou, Y. Liu, S. Pang, T. Zhang, Formation and Properties of Centimeter-Size Zr-Ti-Cu-Al-Y Bulk metallic Glasses as Potential Biomaterials, J. Alloys Compd. 656 (2016) 389–394, <https://doi.org/10.1016/j.jallcom.2015.09.254>.
- [54] A. Inoue, Q.S. Zhang, W. Zhang, K. Yubuta, K.S. Son, X.M. Wang, Formation, Thermal Stability and Mechanical Properties of Bulk Glassy Alloys with a Diameter of 20 mm in Zr-(Ti, Nb)-Al-Ni-Cu System, Mater. Trans. 50 (2009) 388–394, <https://doi.org/10.2320/matertrans.MER2008179>.
- [55] D.C. Hofmann, L.M. Andersen, J. Kolodziejska, S.N. Roberts, J.-P. Borgonia, W.L. Johnson, K.S. Vecchio, A. Kennett, Optimizing Bulk Metallic Glasses for Robust, Highly Wear-Resistant Gears, Adv. Eng. Mater. 19 (2017) 1600541, <https://doi.org/10.1002/adem.201600541>.
- [56] Alfa Aesar: Pure Elements, (2020). <https://www.alfa.com/en/pure-elements/> (accessed November 3, 2020).
- [57] Smart Elements: Pure Elements, (2022). <https://www.smart-elements.com/periodiensystem/> (accessed November 3, 2020).
- [58] K.M. Flores, W.L. Johnson, R.H. Dauskardt, Fracture and fatigue behavior of a Zr-Ti-Nb ductile phase reinforced bulk metallic glass matrix composite, Scr. Mater. 49 (2003) 1181–1187, <https://doi.org/10.1016/j.scriptamat.2003.08.020>.
- [59] D.C. Qiao, G.Y. Wang, P.K. Liaw, V. Ponnambalam, S.J. Poon, G.J. Shiflet, Fatigue behavior of an $Fe_{48}Cr_{15}Mo_{14}Er_{2}C_{15}B_6$ amorphous steel, J. Mater. Res. 22 (2007) 544–550, <https://doi.org/10.1557/jmr.2007.0047>.
- [60] M. Freels, P.K. Liaw, G.Y. Wang, Q.S. Zhang, Z.Q. Hu, Stress-life fatigue behavior and fracture-surface morphology of a Cu-based bulk-metallic glass, J. Mater. Res. 22 (2007) 374–381, <https://doi.org/10.1557/jmr.2007.0052>.
- [61] M.D. Abad, D.J. Browne, An Investigation of the Tribological Behavior of Hf-Based Bulk Metallic Glass and Crystalline Alloys, J. Tribol. 142 (2020) 1–9, <https://doi.org/10.1115/1.4046950>.
- [62] M.Z. Ma, R.P. Liu, Y. Xiao, D.C. Lou, L. Liu, Q. Wang, W.K. Wang, Wear Resistance of Zr-based Bulk Metallic Glass Applied in Bearing Rollers, Mater. Sci. Eng. A. 386 (2004) 326–330, <https://doi.org/10.1016/j.msea.2004.07.054>.
- [63] H.M. Chiu, G. Kumar, J. Blawdziewicz, J. Schroers, Thermoplastic Extrusion of Bulk Metallic Glass, Scr. Mater. 61 (2009) 28–31, <https://doi.org/10.1016/j.scriptamat.2009.02.052>.
- [64] J. Schroers, T.M. Hodges, G. Kumar, H. Raman, A.J. Barnes, Q. Pham, T.A. Wanick, Thermoplastic Blow Molding of Metals, Mater. Today. 14 (2011) 14–19, [https://doi.org/10.1016/S1369-7021\(11\)70018-9](https://doi.org/10.1016/S1369-7021(11)70018-9).
- [65] N. Zhang, J.S. Chu, C.J. Byrne, D.J. Browne, M.D. Gilchrist, Replication of Micro/Nano-Scale Features by Micro Injection Molding with a Bulk Metallic Glass Mold Insert, J. Micromechanics Microengineering. 22 (2012), <https://doi.org/10.1088/0960-1317/22/6/065019> 065019.
- [66] N. Zhang, C.J. Byrne, D.J. Browne, M.D. Gilchrist, Towards Nano-Injection Molding, Mater. Today. 15 (2012) 216–221, [https://doi.org/10.1016/S1369-7021\(12\)70092-5](https://doi.org/10.1016/S1369-7021(12)70092-5).
- [67] S.N. Roberts, Developing and Characterizing Bulk Metallic Glasses for Extreme Applications, PhD Thesis, California Institute of Technology, 2014.